A COGNITIVE COMPENSATION MECHANSIM FOR DEFORMABLE ANTENNAS

A Thesis

by

STEPHEN ANDREW LONG

Submitted to the Office of Graduate Studies of
Texas A&M University
in partial fulfillment of the requirements for the degree of

MASTER OF SCIENCE

May 2009

Major Subject: Electrical Engineering

A COGNITIVE COMPENSATION MECHANISM FOR DEFORMABLE ANTENNAS

A Thesis

by

STEPHEN ANDREW LONG

Submitted to the Office of Graduate Studies of
Texas A&M University
in partial fulfillment of the requirements for the degree of

MASTER OF SCIENCE

Approved by:

Chair of Committee,	Gregory H. Huff
Committee Members,	Robert D. Nevels
	Zoubeida Ounaies
	Takis Zourntos
Head of Department,	Costas N. Georghiades

May 2009

Major Subject: Electrical Engineering

ABSTRACT

A Cognitive Compensation Mechanism for Deformable Antennas. (May 2009)

Stephen Andrew Long, B.S., Texas A&M University at College Station

Chair of Advisory Committee: Dr. Gregory H. Huff

This thesis presents the design, theory, and measurement of a linearly polarized microstrip patch antenna with a novel substrate-integrated mechanism that can compensate the detuning effects from a physical deformation. Specifically, this antenna bends sharply through the center up to 90º (pivoted about the ground plane) and retuning (compensation) occurs by displacing electromagnetically functionalized colloidal dispersions (EFCDs) through a capillary in the substrate (parallel to the radiating edge). The displacement of a high permittivity EFCD by a low permittivity EFCD acts as a net length reduction (shown mathematically using perturbation theory). This mitigates the physical length extension from the deformation and stretching of the conductors. The design can be considered cognitive (conceptually in this thesis) by allowing the deformation and resulting compressive forces in the substrate to actuate displacement.

The antennas to demonstrate this concept have been chosen to operate at 3 GHz and use a Sylgard 184 (a flexible silicone-based elastomer) substrate material with a height of 4 mm. Simulations of an HFSS model demonstrate a stable VSWR 2:1 bandwidth of 141 MHz across the entire range of bending. Currently available fabrication methods and

EFCD material systems provide some limitations. Therefore, proof-of-concept is provided using 2 microstrip patch antennas (one flat patch and one patch bent 90º) designed using 4 mm thick Rochelle Foam substrates and rigid copper sheets. A flexible patch was fabricated using Sylgard 184 and SEC 1233 (a conductive elastomer) but bending created several tears in the material and delaminating of the flexible conductor. However, the comparison of trends between simulated and measured results show good agreement and are used to validate this compensation mechanism.

NOMENCLATURE

EFCD	Electromagnetically Functional Colloidal Dispersion
EMI	Electromagnetic Interference
EMC	Electromagnetic Compatibility
EMV	Electromagnetic Visibility
BSTO	Barium Strontium Titanate
VSWR	Voltage Standing Wave Ratio
PDMS	Polydimethylsiloxane
RHS	Right-hand side

TABLE OF CONTENTS

LIST OF FIGURES

FIGURE Page

FIGURE Page

CHAPTER I

INTRODUCTION

The advent of wireless devices has made an indelible impact on electronic communication systems. In a matter of decades, wireless functionality has been transformed from a novelty into a standard for numerous commercial, personal, and military applications. As a testament to this, many vehicles, handheld devices, and even items of clothing now feature wireless connectivity to enable digital communication in even the most inaccessible environments. At one time these applications featured rigid pole antennas [1]-[3] but the desire to conceal these radiating systems and minimize their weight and aerodynamic profile has became a priority as this application space continues to expand and evolve. Hence, these wireless communication or sensing systems and their antennas must now be conformally integrated into their host structure. A common approach is to layer thin, low-drag, printed antennas on top of the host chassis [4]-[5]. Antenna integration goes even further in the case of smart structures where the antenna often utilizes the structure's conducting surface [6]-[7] and/or the structure utilizes the antenna for mechanical support, making the antenna a structurally functional element of the chassis [8]-[11]. These features expand antenna design and operation into a multidisciplinary practice and a rapidly growing area of research. Potential applications range from body area networks (BANs) on humans [12]-[13] or robotic chassis to

---

This thesis follows the style of *IEEE Transactions on Antennas and Propagation.*

compensate for flexing on joint-areas (e.g., elbows) all the way to morphing aircraft featuring conformal (not simply retrofitted) antennas on wings [14]-[15], the fuselage [16], tailfins [17]-[18], or other aerodynamic control surfaces. Altogether there are numerous areas of interest that are continually evolving.

In a general context, overcoming the electromagnetic interactions (EMI, EMC, coupling, detuning, etc.) between a conformal antenna and its host chassis or superstructure can provide many challenges [19]-[20]. Many future applications involving polymorphic structures (i.e. the hull of a ship warping or an aircraft morphing to different aerodynamic functions) expand this challenge by requiring dynamic solutions that can work in tandem with these system-level operations. Conformal antennas for these smart structures will therefore require flexibility for physical deformation and designs that allow them to operate effectively during these structural changes. Although several antennas feature flexible materials, the performance of a typical antenna deteriorates or changes from the desired operation as it bends [21]-[24]. This illuminates the need for adaptable, or polymorphic, radiating structures that include integrated mechanism to mitigate changes in impedance and/or radiation behavior as a result of shape shifting. An ideal mechanism to counteract these deformations will be cognitive or autonomous and require no outside stimulus other than the deformation itself to perform this function.

Recent developments in dynamic material systems [25]-[27] provide a unique approach to handling dynamic deformation through the use of electromagnetically functionalized

colloidal dispersions (EFCDs). EFCDs are homogeneous mixtures of conductive, magnetic, dielectric, and/or magnetodielectric nanoparticles dispersed in a low-loss non-aqueous fluid media. These EFCDs can be engineered (e.g., functionalized) to have specific electromagnetic properties for the application. Selecting the right colloidal particles and controlling their volume fraction in the EFCD alters the material's electromagnetic properties, thus providing a degree of control over an antenna incorporating the material**.** These technologies are currently being investigated to dynamically alter the material properties within a capillary network to reconfigure a rigid antenna's resonant frequency [27]. The mechanism presented in this work extends this concept into a new direction by physically displacing the EFCDs within a capillary to achieve a compensating mechanism for physical deformation. Consequently, using the deformation to actuate fluid displacement results in a mechanism that cognitively maintains the antenna's performance over various degrees of shape change (much like a fire billow displaces air through compression).

This thesis begins by introducing the important mechanisms and concepts that form the foundation for understanding the antenna design; the theory and operation of a microstrip antenna aid in examining the detuning effects from a localized deformation. This work then examines material perturbation theory to characterize the displacement of EFCDs within the substrate of a patch antenna, which achieves an effect opposing that of the deformation. A proof-of-concept design then utilizes this mechanism to dynamically compensate for a patch antenna bending up to 90º. Simulated models

validate the theoretical considerations as well as the design. Currently available materials and fabrication methods provide measured results that prove the concept and highlight the future needs for electromagnetically functional materials. A summary concludes the work.

CHAPTER II

BACKGROUND

A. *Microstrip Antennas*

Microstrip antennas consist of substrate materials clad with one or more layers of metal. The basic design has a single substrate layer of height *h* with metal on both sides. In the case of a microstrip patch antenna the top layer is etched to form a metal rectangle with a length *L* and width *W*. Current lithography methods allow fast and cost-effective fabrication of patch antennas and arrays. Fig. 1 illustrates a microstrip patch antenna and substrate constitutive parameters.

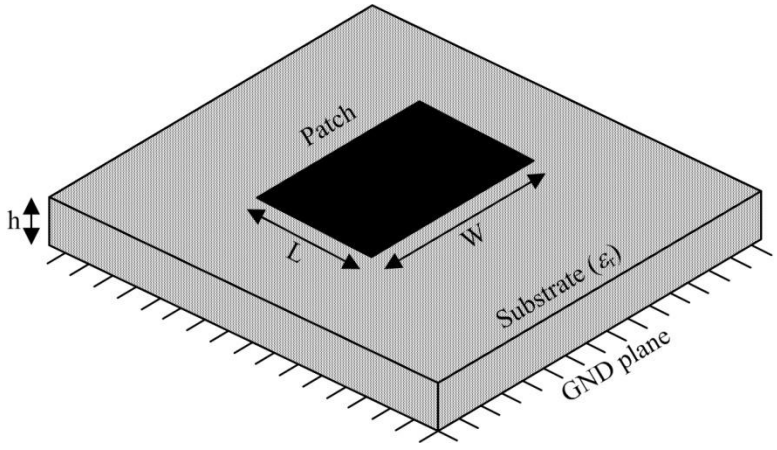

Fig. 1. Physical parameters of a microstrip patch antenna.

Fig. 2 illustrates the typical operation of a patch antenna. The effective cavity formed between the two metal layers and the four vertical side-walls defined by the patch's dimensions has an electromagnetic resonance that allows the antenna to efficiently

transmit power or receive power radiated from other antennas. The resulting electric boundaries (top and bottom) and magnetic boundaries (side-walls) provide the boundary conditions for the electric field underneath the patch and result in a sinusoidal distribution when operating at in one of the resonant modes. The effective length $L_{eff} = L + 2\Delta L$ of the microstrip patch antenna determines the resonant frequency f_0 for the dominant mode. This parameter accounts for the length L, the effective material properties of the substrate (ε_{reff} and μ_{reff}) , and the length extensions $2\Delta L$ from the fringing fields at the edges of the patch. The effective relative permittivity ε_{reff} of the substrate material determines the effective wavelength λ_{eff} according to Eq. (1). From (1), increasing the permittivity of a region increases the number of wavelengths inside, making the region "electrically longer." This allows engineers to design small antennas that resonate at lower frequencies.

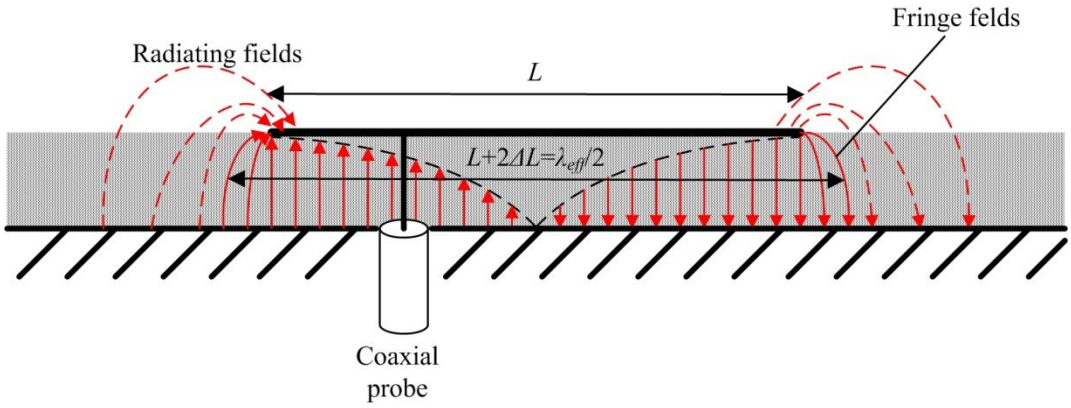

Fig. 2. The TM_{10} electric fields.

$$\lambda_{eff} = \frac{\lambda_0}{\sqrt{\varepsilon_{reff}}} = \frac{c/f}{\sqrt{\varepsilon_{reff}}} \quad (1)$$

Fig. 2 also illustrates the patch antenna's fundamental (resonant) mode - the TM_{10} mode - which has a maximum amplitude of the electric field at both edges and a half-period distribution in between. The fields at these edges are out of phase by 180º (i.e. they point in opposite directions). The coaxial probe inserted into the patch couples electromagnetic energy into this mode. The position of the probe relative to the length of the patch determines the input impedance of the antenna. Fig. 2 also illustrates the *fringing fields* extending from the edges of the antenna. The fringe fields extend outward from the patch, decreasing in strength and becoming the *radiated fields*. The radiating edges at either side of the antenna (separated by the length dimension) are often referred to as *slots*. The 180º phase relationship (e.g., the reversed direction of the z-directed electric field vectors) and the effective distance L_{eff} between these slots determine the radiation pattern of the antenna.

B. *Impedance, VSWR, and Smith Chart*

Measurement of the voltage and current at the input terminals of an antenna determines the input impedance Z_A according to (2). In the general case this complex number is expressed in terms of *resistance* and *reactance*, the real and imaginary components respectively. The impedance of an antenna varies as a function of frequency. The impedance of an antenna determines how much power from a transmission line will

couple into the antenna. The transmission line has a characteristic impedance Z_o (typically 50 Ω). If the antenna has an identical impedance Z_A, the antenna is *matched*, resulting in 100% transmission of the power from the line. If the two impedances are not matched, some or all of the power will reflect at the junction. Not only does reflection reduce the amount of power delivered to the antenna, but enough reflected power can severely damage a network. Since impedance varies with respect to frequency, so does the impedance match. As a result, antennas are typically limited to a specific range of operating frequencies known as the *bandwidth*.

$$Z_A(f) = \frac{V_A(f)}{I_A(f)} = \frac{|V_A(f)|\angle\varphi_V^\circ}{|I_A(f)|\angle\varphi_I^\circ} = \mathrm{Re}(Z_A(f)) + j\,\mathrm{Im}(Z_A(f)) \tag{2}$$

The input reflection coefficient S_{11} characterizes the impedance match of an antenna according to (3) and (4). This value is typically described with a magnitude and phase. Any reflected power results in a standing voltage wave on the transmission line, which is measured as a voltage-standing-wave-ratio (VSWR) according to (5).

$$S_{11} = \frac{Z_A - Z_o}{Z_A + Z_o} = \mathrm{Re}(S_{11}) + j\,\mathrm{Im}(S_{11}) = |S_{11}|e^{j\theta} \tag{3}$$

$$|S_{11}|^2 = \frac{\text{Reflected Power}}{\text{Input Power}} \tag{4}$$

$$VSWR = \frac{1+|S_{11}|}{1-|S_{11}|} \tag{5}$$

From the equations above an ideal impedance match results in S_{11} = 0 and a *VSWR* of 1:1. A *VSWR* of 2:1 indicates that 89% of the input power is delivered to the antenna, an acceptable standard in practical engineering design and the standard used in this work to

define operating bandwidth. Fig. 3 shows the impedance vs. frequency of an ideal resonant antenna. Note that the resistance and reactive curves vary differently with respect to frequency. The coaxial line connected to the antenna has a characteristic impedance of Z_o = 50 Ω, so the antenna impedance must be close to Z_A = 50 Ω, in order to receive any power.

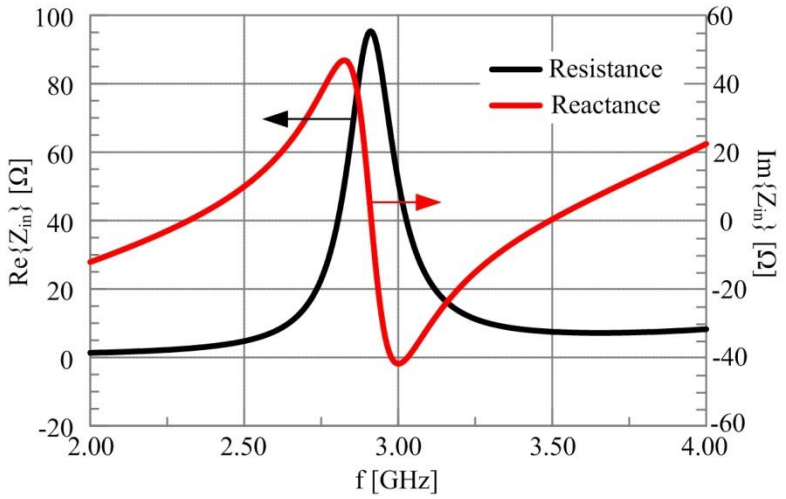

Fig. 3. The impedance of an ideal resonant antenna.

Fig. 4 (left) shows S_{11} of the same antenna plotted on a Smith chart. The center of the chart represents a perfect match and the outer edge represents complete mismatch or 100% reflection. A circle around the center describes a set of values for which $|S_{11}|$ and *VSWR* are constant. The Smith charts in this work include a VSWR 2:1 circle to illustrate bandwidth. Any range of continuous impedance bandwidth that falls within this circle has a VSWR less than 2:1 and meets the desired performance metric. Fig. 4 (right) shows a plot of the VSWR vs. frequency. The 2:1 VSWR bandwidth of this antenna is

151 MHz at a center frequency of f_c = 3 GHz. For this example both the plots of S_{11} and VSWR represent a frequency range of 2 GHz to 4 GHz, but future VSWR plots in this thesis will focus in on the range of 2.5 GHz to 3.5 GHz to make the bandwidth more visible.

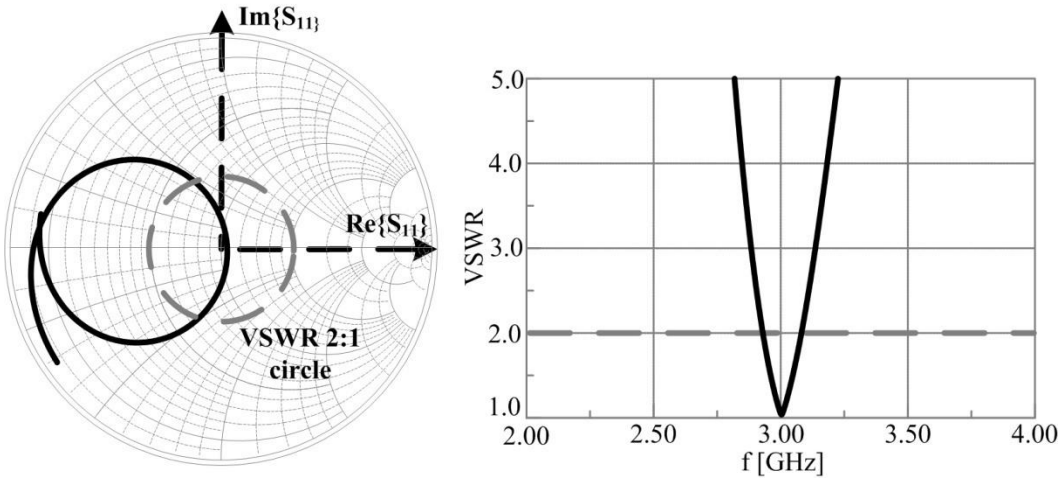

Fig. 4. Smith chart plot of S_{11} (left) and rectangular plot of VSWR (right).

C. EFCD Material Systems

Several different nomenclatures based on the phases of the constituent materials (e.g., solid, liquid, or gas) can describe a colloidal dispersion. This work focuses on the use of solid-liquid dispersions referred to as sols. EFCDs are thus sols that result from the homogeneous dispersion of solid colloidal materials (spherical, magnetodielectric, low-loss particles with a diameter ranging from 1 to 1000 nm) into a low-loss liquid. Fig. 5 shows a conceptual illustration of the EFCDs and mixing rules for a nominal set of materials flowing inside of a capillary structure or fluid channel. Mixing rules can be

extended to include many different materials and also the capillary/channel material, and provide a means to link the contribution of particles at the nano-scale to the antenna's length scale which is wavelength dependent and typically much larger that the colloid's length scale at microwave frequencies.

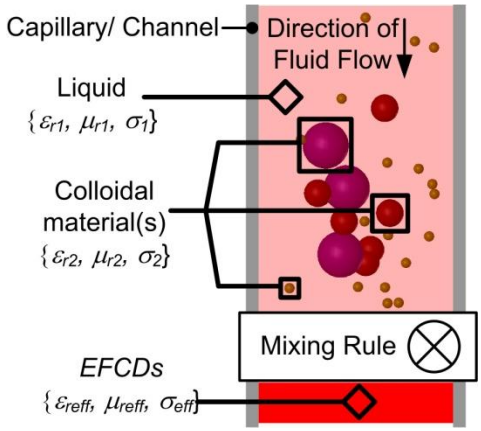

Fig. 5. Illustration of the dynamic material system and the application of mixing rules for colloids dispersed into a liquid (EFCDs) that are flowing down a capillary or fluid channel.

Magnetodielectric compositions of colloidal materials are selected for use in EFCDs based on their ability to alter the local constitutive parameters (ε, μ, and σ) in a device or microfluidic impedance transformer and provide a high degree of electromagnetic agility or electromagnetic visibility (EMV). At the onset of this work, the general Lichtenecker mixing rule [28] was used to approximate the effective material properties of the EFCDs and understand the basic trends given by mixing. As this work matured into fabricated designs and measured results (Chapter IV), the need arose for more accurate mixing rules and material characterization systems. The Maxwell-Garnett mixing rule [29] in (6) accurately calculates the effective EFCD material parameter s_{eff} and provides an intuitive

understanding into how the liquid s_1 and volume fraction ϑ of colloidal material s_2 contribute to the EFCD properties. Since conductive losses are an important factor, s has been used to independently represent the complex properties $s = s\left(1 - j\tan\delta\right)$ (where s can independently represent ε or μ).

$$s_{eff} = s_1 + 3s_1\vartheta\frac{s_2 - s_1}{s_2 + 2s_1 - \vartheta\left(s_2 - s_1\right)} \tag{6}$$

The EFCDs are functionalized by considering the reduction of loss mechanisms and the ability to maintain low viscosities while still using high volume fractions of colloidal material when needed. Ionic dispersants are used in this work to electrostatically stabilize the colloids (e.g., coat them in like-charged, repulsive 'shells'). This mitigates many of the inter-particle forces (Van der Waals, etc.) to avoid aggregation and clotting, but then ionic nature introduces losses. However, achieving high volume fractions would not be possible without these ionic dispersants. Further discussion on this and other means to increase ϑ (e.g., poly-dispersed systems) remains beyond the scope of this thesis but a more in depth description can be found in related literature and books.

CHAPTER III

THEORY

A. Bent Patch Antenna

The comparatively simple topology of the linearly polarized microstrip patch antenna aids in analyzing the effects of both deformation and the compensation mechanism discussed achieved in this work. This thesis examines the effects of a sharp, localized bend in the middle of a patch antenna illustrated in Fig. 6. This deformation differs from the curvature across the whole antenna observed in [24].

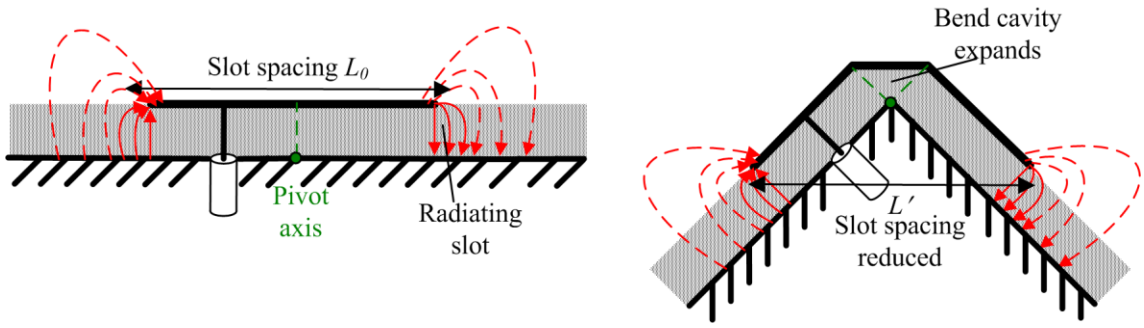

Fig. 6. Operation of a flat microstrip patch antenna (left) and one bent 90° in the middle (right)

This work treats the expansion in the bend region as a physical length extension of the antenna. From an impedance perspective this results in the center frequency of the antenna shifting to the left. Furthermore, a length extension on one side of the feed alters the position of the feed *relative to the original resonant cavity* and alters the input impedance of the antenna. The relative feed location now appears shifted to the edge of

the patch and the impedance loop on Smith chart broadens. The impedance match of the antenna then deteriorates and this decrease in bandwidth and the shift in the center frequency severely detunes the antenna.

Deformation also affects the radiation mechanism of the microstrip patch antenna. In the case of a linearly polarized patch, the mechanism consists of an array of radiating slots (the two edges of the patch separated by the length L_{eff}). Initially the slots are a distance $L_0 = \lambda_{eff}/2$ apart from one another. Fig. 6 shows the decrease in physical separation when the antenna folds. From array theory [30], decreasing slot separation results in broadening of the radiation pattern. In addition, the slots are initially 180° out of phase at the operating frequency, but the length extension of the resonant cavity distorts this phase. This is analogous to applying a progressive phase shift in an array which tilts the radiation pattern off axis.

B. EFCD Capillary

Given the length-extending behavior of bend, the compensation mechanism (in this work) should provide a length-reducing effect. Furthermore, the equivalent length reduction should occur on the same side of the probe as the bend in order to preserve the relative location of the feed (for impedance matching purposes). This work considers an EFCD-filled capillary to achieve this - displacing EFCDs within a substrate-embedded capillary to act as a localized material perturbation that can compensate bending. From material perturbation theory [31], decreasing the permittivity in a localized region of the

antenna achieves this effect - particularly within regions of maximum electric field. Ergo, displacing a high permittivity EFCD with a low permittivity EFCD lowers the aggregate permittivity of the substrate and makes the antenna element look "electrically shorter."

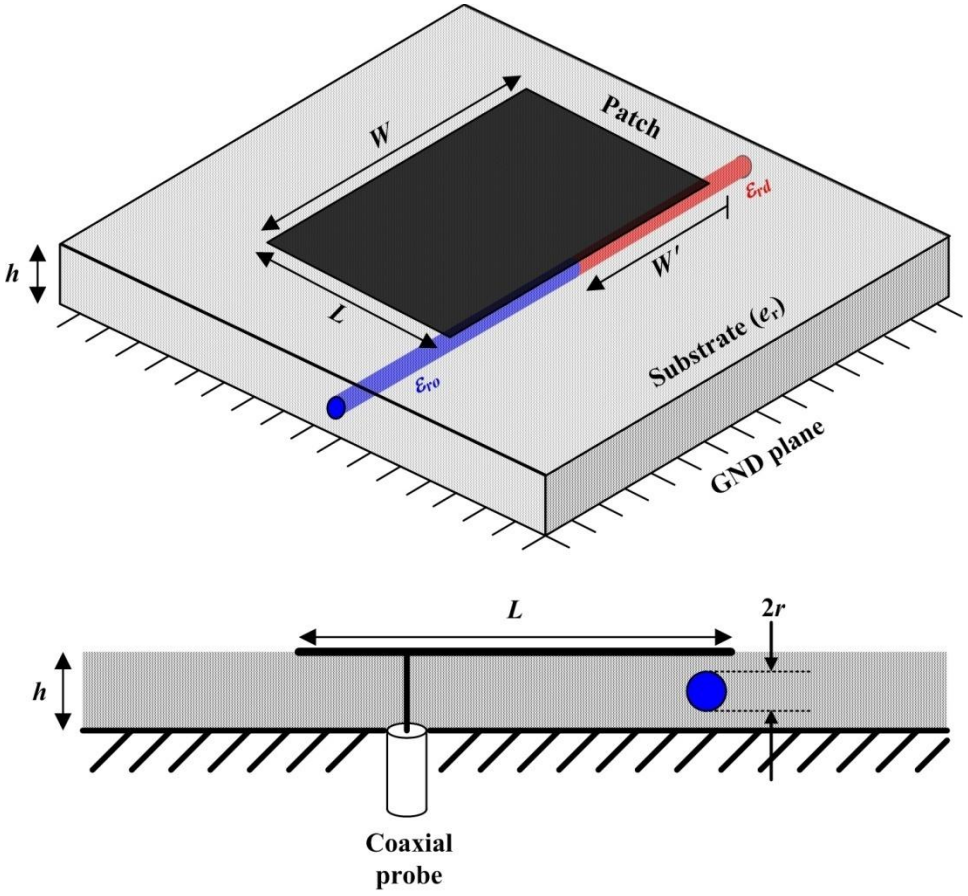

Fig. 7. EFCD displacement within a substrate capillary.

Fig. 7 illustrates the displacement of these two EFCDs underneath the patch antenna. The difference in EFCD permittivity, the displacement volume, and the relative strength of the electric field in the perturbation region link multiple degrees of freedom for

controlling this effect. Eq. (7) quantifies the change in a cavity's resonant frequency as a result of material perturbation, where $\vec{E}_0$ and $\vec{H}_0$ represent the initial electric and magnetic fields within the cavity, and $\vec{E}$ and $\vec{H}$ represent the fields after a material displacement. $\Delta\varepsilon$ and $\Delta\mu$ are the respective changes in the cavity material's permittivity and permeability. For electrically small perturbations in which the field structure remains fundamentally unchanged (e.g., they are identical to a microstrip patch with no capillary the material perturbation) – shown in (8) – the expression in (7) reduces to (8).

$$\frac{f-f_0}{f_0} \approx -\frac{\iiint_{cavity}\left(\Delta\varepsilon\vec{E}\bullet\vec{E}_0^{*}+\Delta\mu\vec{H}\bullet\vec{H}_0^{*}\right)d\tau}{\iiint_{cavity}\left(\varepsilon\vec{E}\bullet\vec{E}_0^{*}+\mu\vec{H}\bullet\vec{H}_0^{*}\right)d\tau} \tag{7}$$

$$\begin{aligned}\vec{E} &\approx \vec{E}_0 \\ \vec{E}\bullet\vec{E}_0^{*} &= \left|\vec{E}_0\right|^2\end{aligned} \tag{8}$$

$$\frac{f-f_0}{f_0} \approx -\frac{\iiint_{cavity}\left(\Delta\varepsilon\left|\vec{E}_0\right|^2+\Delta\mu\left|\vec{H}_0\right|^2\right)d\tau}{\iiint_{cavity}\left(\varepsilon\left|\vec{E}_0\right|^2+\mu\left|\vec{H}_0\right|^2\right)d\tau} \tag{9}$$

Evaluation of (9) for the rectangular cavity created by the microstrip patch antenna yields (10); since the EFCD is non-magnetic, $\Delta\mu = 0$ and the expression reduces to (11).

$$\frac{f-f_0}{f_0} \approx -\frac{\int_{z=0}^{h}\int_{y=0}^{W}\int_{x=0}^{L}\left(\Delta\varepsilon\left|\vec{E}_0\right|^2+\Delta\mu\left|\vec{H}_0\right|^2\right)dxdydz}{\int_{z=0}^{h}\int_{y=0}^{W}\int_{x=0}^{L}\left(\varepsilon\left|\vec{E}_0\right|^2+\mu\left|\vec{H}_0\right|^2\right)dxdydz} \tag{10}$$

$$\frac{f-f_0}{f_0} \approx -\frac{\int_{z=0}^{h}\int_{y=0}^{W}\int_{x=0}^{L} \Delta\varepsilon \left|\vec{E}_0\right|^2 dxdydz}{\int_{z=0}^{h}\int_{y=0}^{W}\int_{x=0}^{L} \left(\varepsilon\left|\vec{E}_0\right|^2 + \mu\left|\vec{H}_0\right|^2\right) dxdydz} \tag{11}$$

$\vec{E}_o$ and $\vec{H}_o$ can be expressed as mode vectors and mode voltages/currents. Because the patch substrate thickness is so small in terms of wavelengths, the fields across the cavity height are approximately uniform, eliminating a *z* dependence. This means the mode functions describe distribution in *x* and *y* only.

$$\begin{aligned} \vec{E}_0 &= \vec{E}_{m,n} = \vec{e}_{m,n}(\mathrm{x,y})\mathrm{V_{m,n}} \\ \vec{H}_0 &= \vec{H}_{m,n} = \vec{h}_{m,n}(\mathrm{x,y})\mathrm{I_{m,n}} \end{aligned} \tag{12}$$

Where $\vec{e}_{m,n}$ and $\vec{h}_{m,n}$ are the modal vectors that specify specific distributions of the fields according to the cavity's boundary conditions. The indices *m* and *n* describe the order of the mode in the x and y directions respectively. $V_{m,n}$ and $I_{m,n}$ are the mode voltages and currents respectively. These field-vectors are normalized using the orthogonality relationship in (13) where $\mathrm{V_{m,n}} = 1$ V and/or $\mathrm{I_{m,n}} = 1$ A. This expression normalizes the energy and power in the cavity, where $\vec{\mathrm{e}}_{\mathrm{m,n}}$ and $\vec{\mathrm{h}}_{\mathrm{m,n}}$ are the mode vectors normalized to 1, and $\delta_{m,n}$ and $\gamma_{m,n}$ are the constants that normalize the integral to 1.

$$\begin{aligned} \iiint \varepsilon\left(\vec{e}_m \bullet \vec{e}_n^{\,*}\right)d\tau &= \iiint \varepsilon\left(\vec{e}_{m,n}\right)^2 d\tau = \iiint \varepsilon\delta_{m,n}\left(\vec{\mathrm{e}}_{\mathrm{m,n}}\right)^2 d\tau = 1 \\ \iiint \mu\left(\vec{h}_m \bullet \vec{h}_n^{\,*}\right)d\tau &= \iiint \mu\left(\vec{h}_{m,n}\right)^2 d\tau = \iiint \mu\gamma_{m,n}\left(\vec{\mathrm{h}}_{\mathrm{m,n}}\right)^2 d\tau = 1 \end{aligned} \tag{13}$$

The expression above states that integrated energy for all modes is the same, and this may be expressed as:

$$\iiint_{cavity} \varepsilon \left|\vec{E}_0\right|^2 d\tau = 1$$
$$\iiint_{cavity} \mu \left|\vec{H}_0\right|^2 d\tau = 1 \tag{14}$$

$$\varepsilon \left|E_o\right|^2 = \varepsilon \left|E_{m,n}\right|^2 = \varepsilon\delta_{m,n} \left|\vec{\mathrm{e}}_{\mathrm{m,n}}(\mathrm{x,y})\right|^2$$
$$\mu \left|H_o\right|^2 = \mu \left|H_{m,n}\right|^2 = \mu\gamma_{m,n} \left|\vec{\mathrm{h}}_{\mathrm{m,n}}(\mathrm{x,y})\right|^2 \tag{15}$$

In the case of a microstrip patch antenna *without a capillary* and magnetic fields transverse to the direction of propagation (i.e. a $TM_{m,n}$ mode) the boundary conditions of the cavity enforce

$$\vec{e}_{m,n}(x,y) = \hat{z}\cos\left(\frac{m\pi x}{L}\right)\cos\left(\frac{n\pi y}{W}\right) \qquad \begin{matrix} 0 \le x \le L \\ 0 \le y \le W \end{matrix} \tag{16}$$

From the expression above, *m* and *n* determine the number of half-periods of the distribution in the *x* and *y* directions respectively. Fig. 2 in the background section shows the TM_{10} mode. Solving for the normalization factor $\delta_{m,n}$ in the general $TM_{m,n}$ case of a microstrip patch antenna results in

$$\iiint_{cavity} \delta_{m,n} \left|\vec{\mathrm{e}}_{\mathrm{m,n}}\right|^2 d\tau = \int_{z=0}^{h}\int_{y=0}^{W}\int_{x=0}^{L} \delta_{m,n}\left(\cos\left(\frac{m\pi x}{L}\right)\cos\left(\frac{n\pi y}{W}\right)\right)^2 dxdydz = 1 \tag{17}$$

Because the normalization factor is a constant and the modal function is not dependent on *z*. Solving for the normalization factor and evaluating for (*m*, *n*) = (1, 0) gives

$$\delta_{m,n} = \frac{1}{h\int_{y=0}^{W}\int_{x=0}^{L}\left(\cos\left(\frac{m\pi x}{L}\right)\cos\left(\frac{n\pi y}{W}\right)\right)^2 dxdy} = \frac{4}{h\cdot W\cdot L} \tag{18}$$

There is no need to solve for γ because as a result of (14) the magnetic energy integral is interchangeable with the electric energy integral. Because the permittivity change $\Delta\varepsilon$ only occurs in the region of the capillary, the integrated volume in the right-hand side (RHS) numerator reduces to the displaced cylindrical volume within the capillary. Because this volume experiences a homogenous $\Delta\varepsilon$, this term is brought outside the integral and rewritten as a difference. Expressing the RHS in terms of relative permittivities gives (19), where r is the capillary radius, z' is along the width of the patch, and W' is the distance of the displacement (e.g., how much fluid is displaced). ε_{ro} is the relative permittivity of the EFCD initially in the capillary and ε_{rd} is the relative permittivity of the material displacing it. Note that the order has been switched to change the sign in front of the expression. ε_{rs} is the relative permittivity within the entire cavity, including the capillary. The material composition of the cavity is not uniform, so ε_{rs} is a function of position.

$$\frac{\left(\varepsilon_{ro}-\varepsilon_{rd}\right)\int_{z'=0}^{W'}\int_{\phi=0}^{2\pi}\int_{\rho=0}^{r}\left|\vec{E}_0\right|^2\rho d\rho d\phi dz'}{2\int_{z=0}^{h}\int_{y=0}^{W}\int_{x=0}^{L}\varepsilon_{rs}\left|\vec{E}_0\right|^2 dxdydz} \qquad \begin{matrix} 0\le W'\le W \\ 0\le r\le \dfrac{h}{2}\end{matrix} \tag{19}$$

A few reasonable assumptions based on the model simplify the expression in both the numerator and the denominator. The first assumes a small capillary diameter and placement along the edge of the patch. This removes the ρ and ϕ dependence from $\vec{E}_0$ in the numerator (i.e. the modal electric field is treated as uniform across the cross section of the capillary) of (19); Fig. 8 illustrates this approximation. Furthermore, the modal

distribution and normalization factor have no variation in the y-direction for the TM_{10} mode, This removes the z' dependence from $\vec{E}_o$. These approximations yield (20).

$$\frac{\left(\varepsilon_{ro}-\varepsilon_{rd}\right)\left|\vec{E}_0\right|^2\left(W'\pi r^2\right)}{2\int_{z=0}^{h}\int_{y=0}^{W}\int_{x=0}^{L}\varepsilon_{rs}\left|\vec{E}_0\right|^2 dxdydz} \tag{20}$$

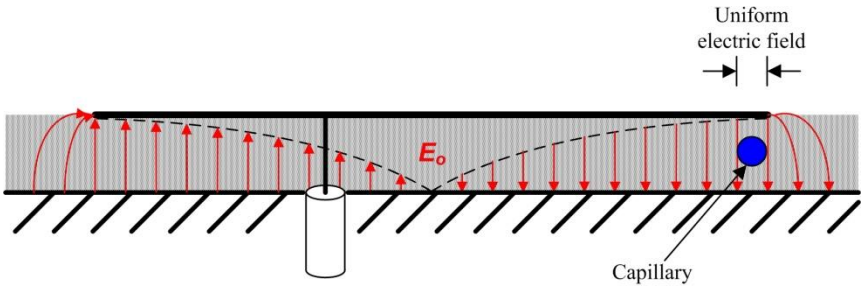

Fig. 8. Small capillary assumption

Also from the small capillary assumption, the volume of the capillary is insignificant compared to the volume of the entire cavity, implying the net energy in the cavity is mostly unaffected by the capillary. This also suggests that the presence of the capillary, as well as displacement within it, does not significantly alter the modal function of the electric field. In other words the small capillary assumption reiterates (8). From this (14) replaces the integral in the denominator in (20).

$$\frac{f-f_o}{f_o}\approx\frac{1}{2}\left(\varepsilon_{ro}-\varepsilon_{rd}\right)\left|E_o\right|^2\left(W'\pi r^2\right) \tag{21}$$

Substituting (15) into the expression above gives an approximation for the TM_{10} frequency shift

$$\frac{f-f_o}{f_o}\approx 2\left(\varepsilon_{ro}-\varepsilon_{rd}\right)\cos^2\left(\frac{\pi x'}{L}\right)\frac{\left(W'\pi r^2\right)}{\left(W\cdot L\cdot h\right)} \qquad \begin{matrix} 0\le x'\le L \\ 0\le W'\le W \\ 0\le r\le h/2 \end{matrix} \tag{22}$$

where x' is the position of the capillary along the length of the patch. According to (22) the frequency shift is proportional to the ratio of displaced volume to the cavity volume and is a maximum when $x' = 0$ or $x' = L$. While these trends seem reasonable, the linear relationship to permittivity change implies this frequency shift does not approach a limit.

The small capillary assumption for the electric field in the capillary did not account for a potential difference in the electric field strength between the inside and outside of the capillary. The assumption simply set the electric fields in the capillary equal to the electric fields in the same region of a normal microstrip patch antenna. However, from [32] the fields inside a long thin dielectric cylinder are related to the external fields by (23). This expression applies to a dielectric cylinder in air ($\varepsilon_{r,ext} \sim 1$), but this thesis rewrites (23) to describe a dielectric cylinder surrounded by a different dielectric medium. This results in the expression shown in (25).

$$E_{\text{int}} = \frac{2}{1+\varepsilon_r} E_{ext} \tag{23}$$

$$E_{\text{int}} = \frac{2}{1+\dfrac{\varepsilon_{r,\text{int}}}{\varepsilon_{r,ext}}} E_{ext} \tag{24}$$

$$E_{capillary} = \frac{2}{1+\dfrac{\varepsilon_{ro,rd}}{\varepsilon_{rs}}} E_0 \tag{25}$$

The initial assumptions about field-structure are still in place with this approximation about the magnitude of the field and the denominator in the material perturbation expression is left alone because the integral of the fields in the entire cavity is still

assumed to be unchanged from the presence of the capillary. The normalized modal function $\vec{e}_{m,n}$ of the cavity also remains unchanged. The electric fields are still assumed to be uniform in the cross-section of the capillary. These assumptions mean this correction only inserts coefficients inside the numerator. Rewriting (7) with these coefficients provides (26) and with this correction for the new magnitude of the electric fields in the TM_{10} the frequency shift can be approximated by (27).

$$\frac{f-f_0}{f_0} \approx -\frac{\int_{z=0}^{W'}\int_{\phi=0}^{2\pi}\int_{\rho=0}^{r} \Delta\varepsilon \left(\frac{2}{1+\frac{\varepsilon_{rd}}{\varepsilon_{rs}}}\vec{E}_0 \bullet \frac{2}{1+\frac{\varepsilon_{ro}}{\varepsilon_{rs}}}\vec{E}_0 \right) dxdydz}{2\int_{z=0}^{h}\int_{y=0}^{W}\int_{x=0}^{L} \varepsilon \left|\vec{E}_0\right|^2 dxdydz} \tag{26}$$

$$\frac{f-f_o}{f_o} \approx \frac{4\varepsilon_{rs}\left(\varepsilon_{ro}-\varepsilon_{rd}\right)}{{\varepsilon_{rs}}^2+\varepsilon_{ro}\varepsilon_{rd}+\varepsilon_{rs}\varepsilon_{ro}+\varepsilon_{rs}\varepsilon_{rd}} \cos^2\left(\frac{\pi x'}{L}\right)\frac{\left(W'\pi r^2\right)}{\left(W\cdot L\cdot h\right)} \tag{27}$$

A function of three different material permittivities now replaces the linear dependence on $\Delta\varepsilon$ from in (22). Taking a specific case where $x' = L = 40.5$ mm, $W' = W$, $h = 4$ mm, and $r = 1.5$ mm helps examine the trends and limits of frequency shift resulting from variations in the material properties. From these dimensions, (27) reduces to (28) and Figs. 9-11 have been provided to examine a family of curves that examines the impact of these different material-based parameters.

$$\frac{f-f_0}{f_0} \approx .1746\frac{\varepsilon_{rs}\left(\varepsilon_{ro}-\varepsilon_{rd}\right)}{{\varepsilon_{rs}}^2+\varepsilon_{ro}\varepsilon_{rd}+\varepsilon_{rs}\varepsilon_{ro}+\varepsilon_{rs}\varepsilon_{rd}} \tag{28}$$

Fig. 9 shows the relative shift in frequency vs. ε_{rd} when ε_{ro} and ε_{rs} are set to static values. In all cases of ε_{ro} and ε_{rs}, the maximum frequency shift occurs when $\varepsilon_{rd} = 1$, or when air

is pumped into the capillary. This trend is intuitive since $\varepsilon_{rd} = 1$ represents the largest $\Delta\varepsilon$. Note that as ε_{rd} approaches ε_{ro} the shift becomes negative. Fig. 10 shows the shift in frequency vs ε_{ro} when $\varepsilon_{rd} = 1$, and ε_{rs} is set to nominal static values based common substrate permittivities. The curves all demonstrate asymptotic behavior; the frequency shift approaches a limit. In this example the limit and the rate at which the limit is approached depends solely on the substrate permittivity ε_{rs}.

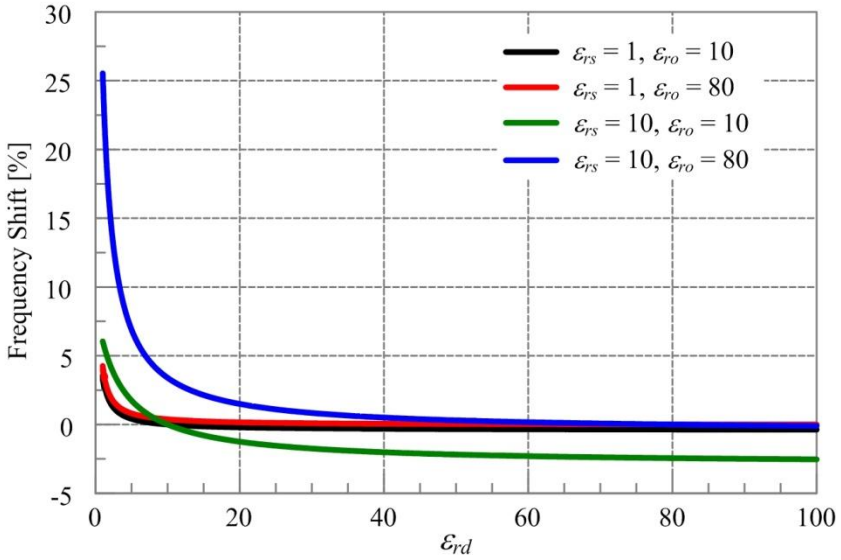

Fig. 9. Frequency shift [%] vs permittivity of material pumped in.

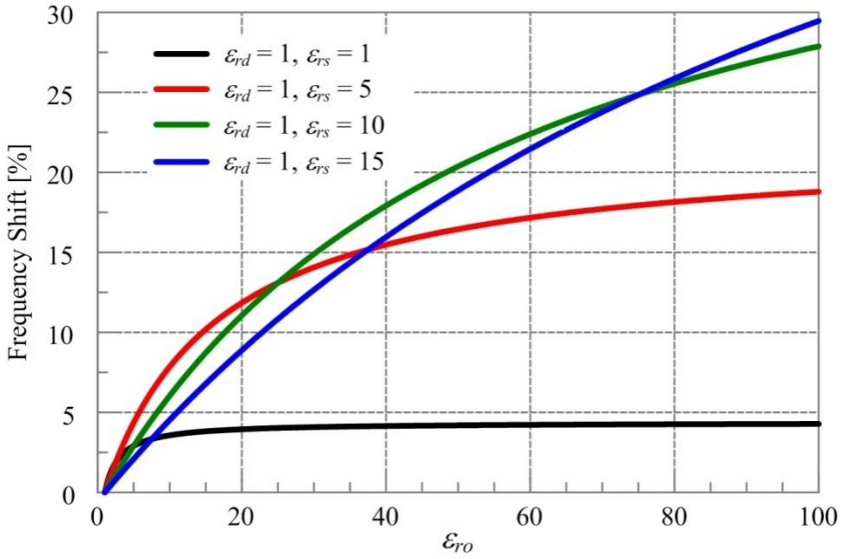

Fig. 10. Frequency shift [%] vs permittivity of material pumped out.

Fig. 11 illustrates the same shifts of Fig. 10 but replaces the horizontal axis to represent the volume fraction ϑ of an EFCD. The EFCD in this example consists of colloids with ε_{r1} = 500 dispersed in a liquid with ε_{r2} = 2.4 and the effective permittivity ε_{ro} is calculated using the Maxwell-Garnett mixing rule in (6).

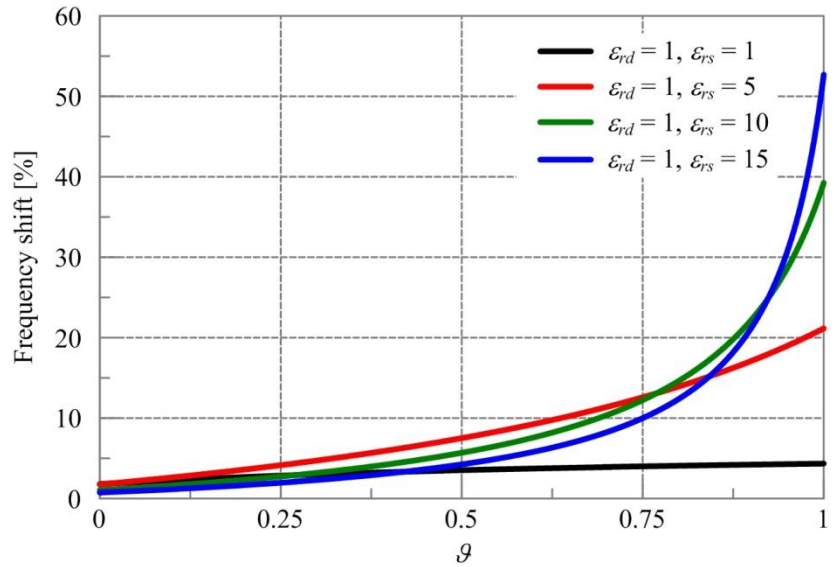

Fig. 11. Frequency shift [%] vs volume fraction of EFCD.

Fig. 12 shows the shift in frequency vs ε_{rs} when ε_{rd} = 1, and ε_{ro} is set to nominal static values based on potential permittivities of EFCDs currently in development. The curve would suggest that there is an optimum substrate permittivity ε_{rs} when designing the antenna, but altering ε_{rs} results in altering L which would alter the ratio of displaced volume to the cavity volume for which the curve is normalized to. While not a useful trace for design, the figure provides insight into the interaction of material properties with the frequency shift. From (25), a very low ε_{rs} results in a low value for $E_{capillary}$ and a weaker perturbation. For a very large $\varepsilon_{rs,}$ the ε_{rs}^2 term becomes the dominant term in the denominator of (27) and also results in a weakened perturbation..

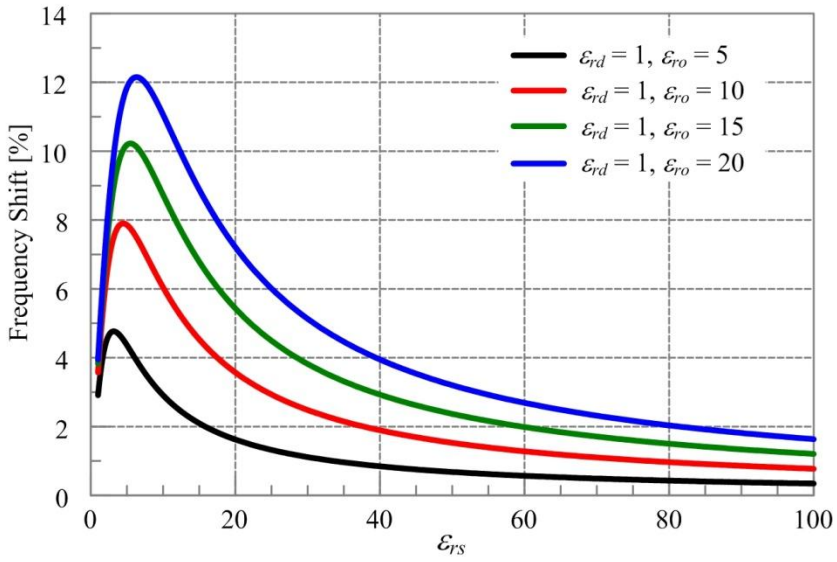

Fig. 12. Frequency shift [%] vs permittivity of substrate.

C. "Billowing" Mechanism

In order for the material compensation to cognitively respond to physical deformation, the bending of the antenna has been assumed to actuate the EFCD displacement. Though no specific apparatus is discussed, this thesis assumes a reservoir of the lower permittivity material rests below the ground plane and is compressed as the ground plane bends. This compression forces the low permittivity material (shown below in red) through a capillary network that runs through the antenna's substrate. Fig. 13 illustrates the substrate-integrated compensation mechanism (which can be conceptually described as a fire billow)in action. The mechanism features all the degrees of freedom of the EFCD capillary: material permittivities, capillary radius r, capillary location x', and capillary displacement W'. $L_1 + L_2$ is the length of the antenna in the flat state and the length dL represents the physical extension of the patch as a result of bending.

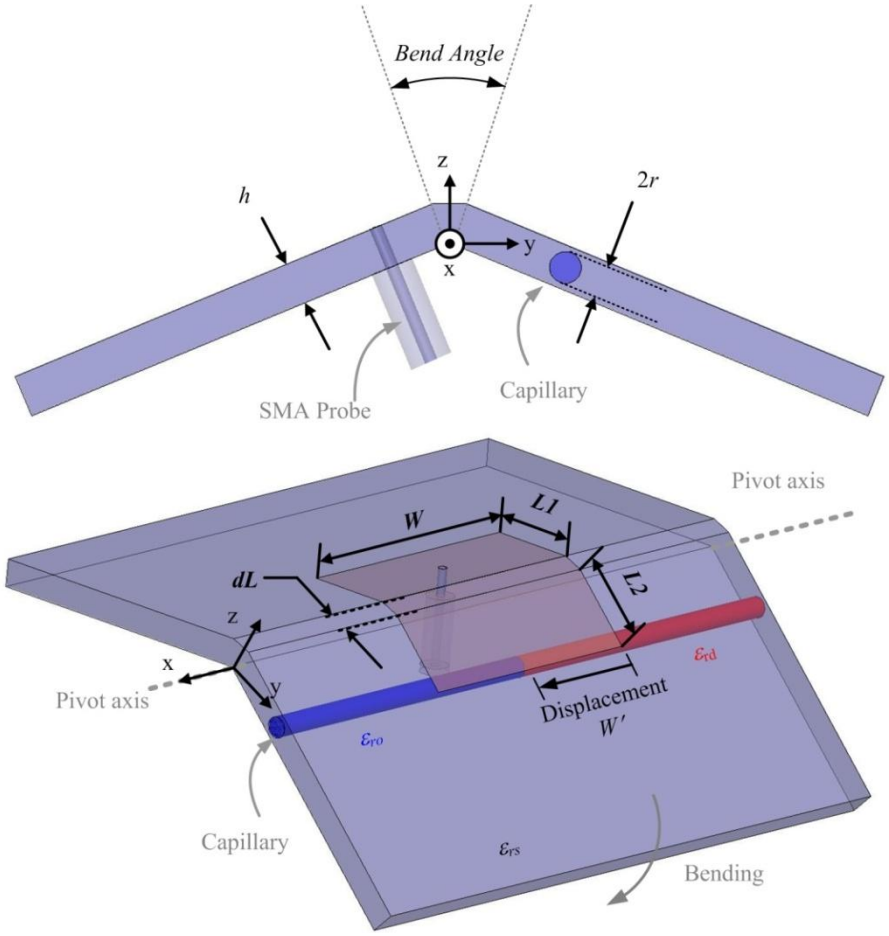

Fig. 13. EFCD-compensated bent patch antenna.

CHAPTER IV

FABRICATED ANTENNA AND RESULTS I

A. Simulation

A microstrip patch antenna was modeled in EM simulation software [33] in order to validate the theoretical considerations. Fig. 14 below illustrates the model used to study the effects of deformation.

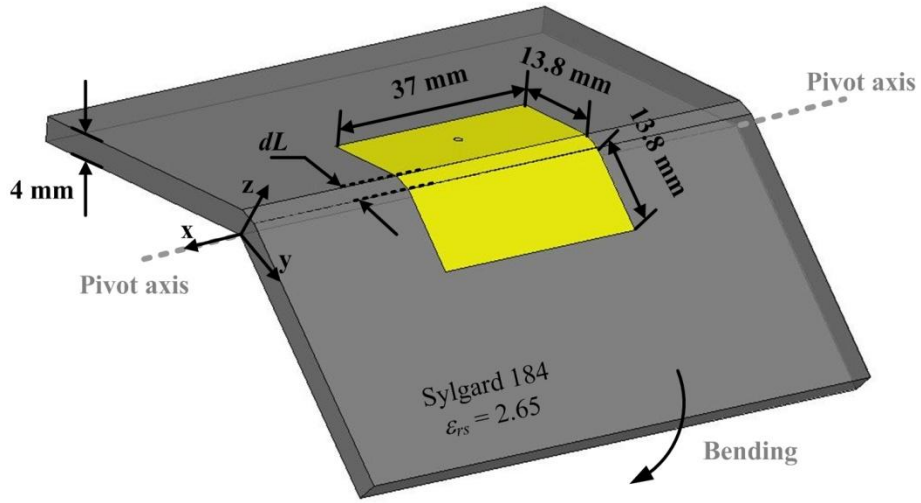

Fig. 14. Simulated model of a bent patch antenna.

Sylgard 184 [34], a silicone-based elastomer, was selected for the substrate because of its durability and elasticity as well as other useful dielectric properties. The dimensions of the model shown in Fig. 14 are h = 4 mm, W = 37 mm, L = 27.6 mm. The antenna is probe-fed 6.5 mm from the back edge. Fabrication methods and EFCD material systems at the time provided a basis for determining the substrate height and capillary diameter. The other dimensions including the feed location are based on design equations and

tuned for a flat microstrip patch antenna operating at f_o = 3 GHz. The model bends in the middle, expanding a bend region. Fig. 15 shows the impedance effects of deformation. The Smith chart in Fig. 15 (left) shows the impedance locus broadening as the antenna bends, detuning the impedance match. The VSWR plot in Fig. 15 (right) provides further illustration as the trace shifts up (degradation in impedance match) and to a lower center frequency. The antenna detunes entirely out of its original bandwidth when the bend is only 45º.

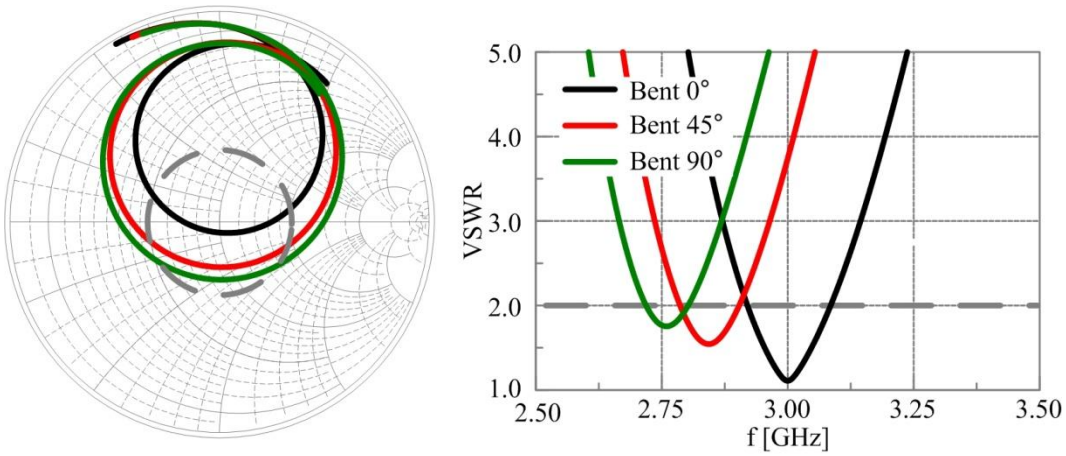

Fig. 15. Smith chart showing S_{11} for the patch antenna bending 0º, 45º and 90º (left) and corresponding VSWR (right).

Fig. 16 shows the detuning of a flat microstrip patch antenna as length is added on one side of the probe. The similar trends in VSWR curves and impedance loci validate the treatment of the deformation as a length extension.

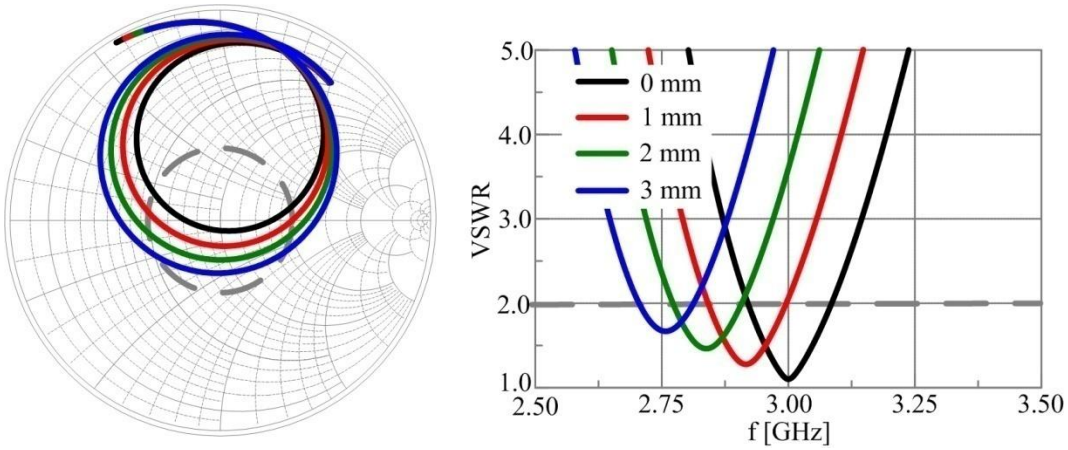

Fig. 16. Smith chart showing S_{11} for the patch antenna with a length extension (left) and corresponding VSWR (right).

The radiation patterns of the antenna for f_o = 3 GHz are shown in Fig. 17. The patterns ignore the impedance mismatch as a result of detuning in order to focus on pattern shape change. The patterns in both plains broaden as a result of a 90º bend, reducing the directivity of the antenna. In the y-z plane the radiation pattern is centered off of broadside despite the symmetrical nature of the deformation and the cross-polarization rises nearly 10 dB.

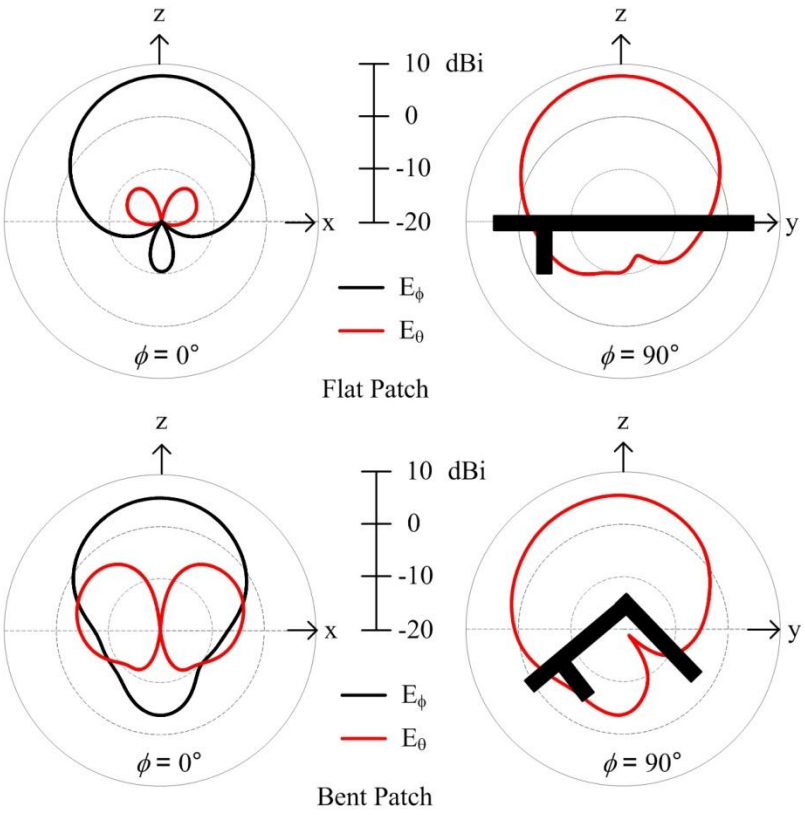

Fig. 17. Radiation patterns for a flat patch antenna (top) and a bent patch antenna (bottom).

A flat microstrip patch antenna with a capillary (see Fig. 7) of radius r = 1.5 mm was simulated to verify the impedance effects of EFCD displacement. The radius represents EFCD-filled straws developed for the experiment. The basic antenna dimensions resemble the antenna without the capillary except the length of the patch has been trimmed to L = 24.8 mm to provide an impedance match when the high permittivity material (ε_{ro} = 25) is initially present. The nominal value chosen for ε_{ro} is a result of ambitious material considerations made at the onset of this work. The material pumped into the capillary is air ($\varepsilon_{rd} \sim 1$).

Fig. 18 shows the impedance effects of replacing the EFCD in the capillary with air. Each curve represents a different fraction of the high permittivity material being displaced (e.g. 75% corresponds to $W' = .75W$).

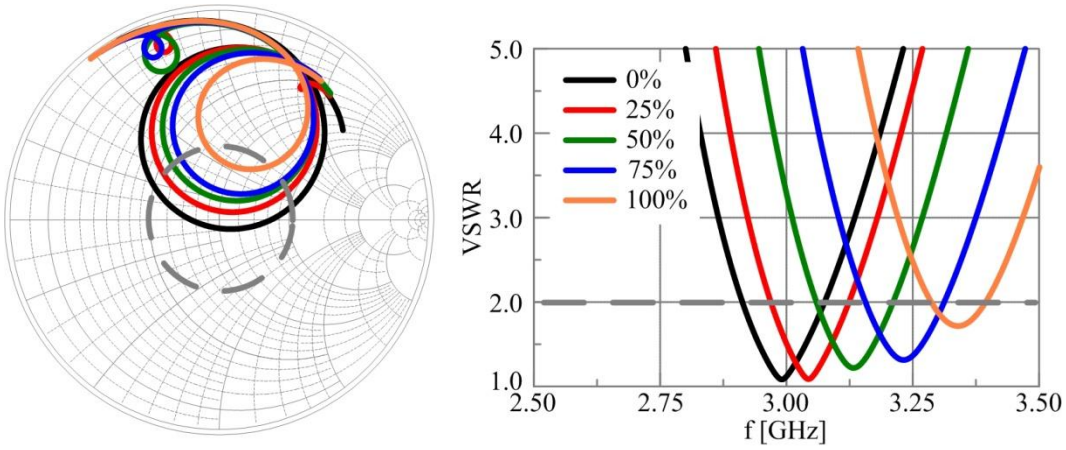

Fig. 18. Smith chart showing S_{11} for the patch antenna with EFCD displacement (left) and corresponding VSWR (right).

The center frequency increases and the Smith chart locus contracts, trends which oppose those observed with the deformation and validate the treatment of the EFCD displacement as an electrical length reduction. The secondary loci in the Smith chart represent additional modes excited when both the EFCD and air are present in the capillary. The modes occur between 2.2 GHz and 2.3 GHz, far enough away from the operating band to exceed the scope of this study. In addition these modes have a VSWR > 7:1.

Some variations of the EFCD capillary's operation and placement evaluate the the theoretical considerations made earlier. Figs. 19 and 20 show the results for EFCD displacements outside the rectangular volume directly beneath the patch antenna.

Because the electric fields are so confined to the cavity, these material perturbations have negligible effects.

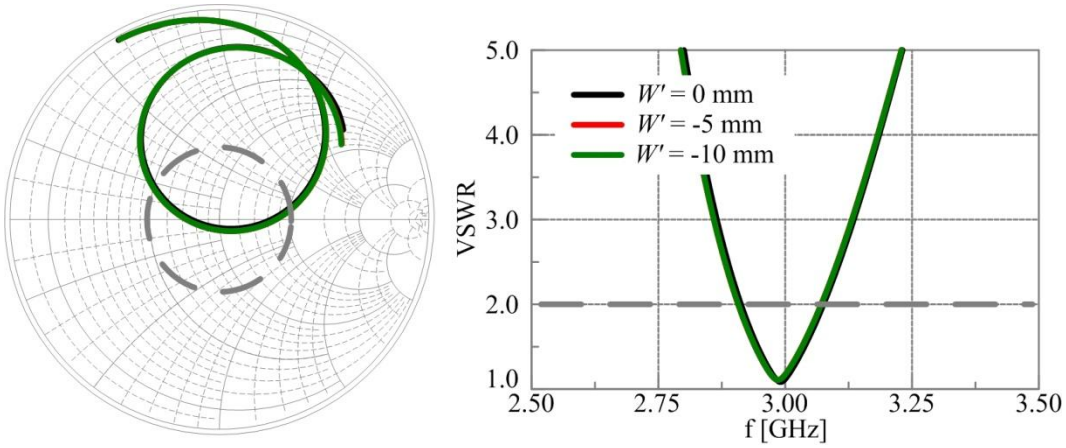

Fig. 19. Smith chart showing S_{11} for the case of $W' \leq 0$ (left) and corresponding VSWR (right).

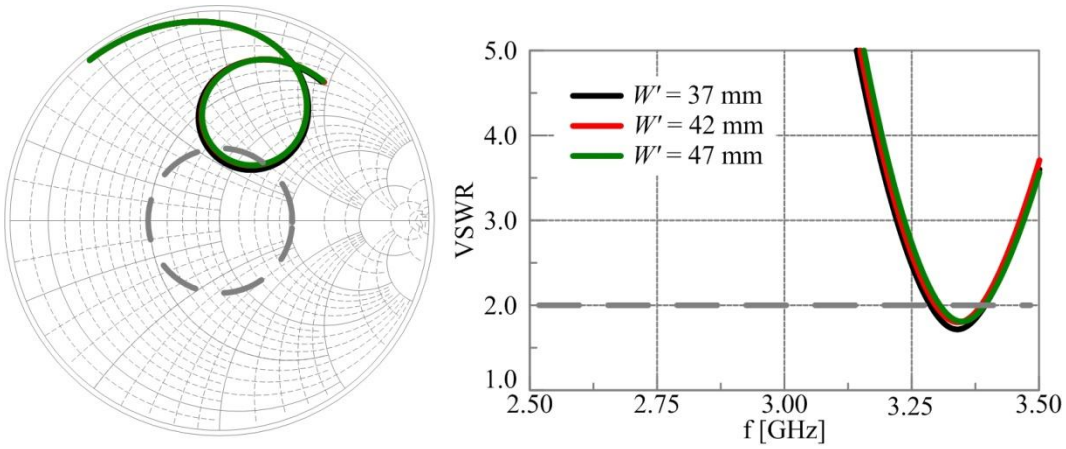

Fig. 20. Smith chart showing S_{11} for the case of $W' \geq W$ (left) and corresponding VSWR (right).

From the cavity model of the patch antenna the electric fields are weakest in the center of the patch. Fig. 21 illustrates the result of placing the capillary in the middle of the patch. The dramatic shift in center frequency from a 25% displacement challenges the

theoretical considerations of the model. The Smith chart locus for the initial state begins to curve back toward the center, suggesting another resonant mode at a higher frequency may be present. The modal distribution for this new resonance is not examined since it disappears when the EFCD is displaced 25%. After 25% displacement there is little or no shift in the impedance behavior validating the assertion that the electric fields in the center of the patch are weak and the patch is operating in the TM_{10} mode.

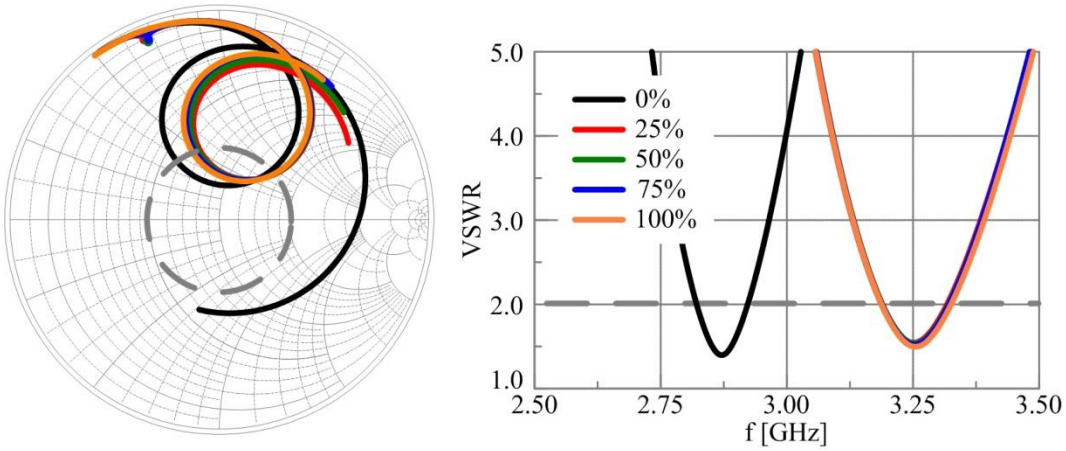

Fig. 21. Smith chart showing S_{11} for the EFCD capillary located in the middle of the patch (left) and corresponding VSWR (right)

The patch featuring the EFCD capillary is modified to feature a bend in the middle as well (see Fig. 6). Parametric analysis tunes W' to provide the best impedance match for each bend angle. The displacements which produce the best possible match are listed in Fig. 22. The results in Fig. 22 indicate the compensation mechanism is functional as the antenna does not significantly detune despite the deformation. The antenna preserves 151 MHz of functional bandwidth across all three bend angles. Fig. 23 shows the radiation patterns of the EFCD-modified bent patch.

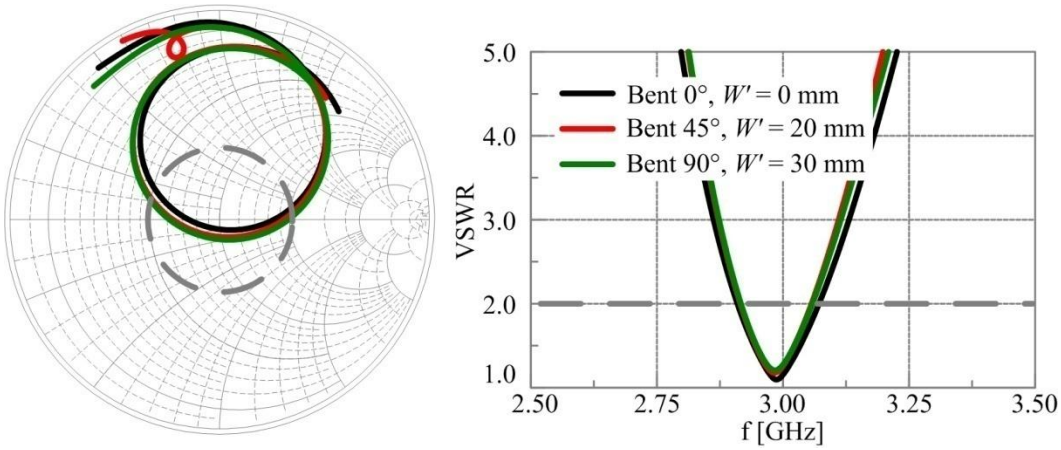

Fig. 22. Smith chart showing S_{11} for the EFCD-compensated antenna (left) and corresponding VSWR (right).

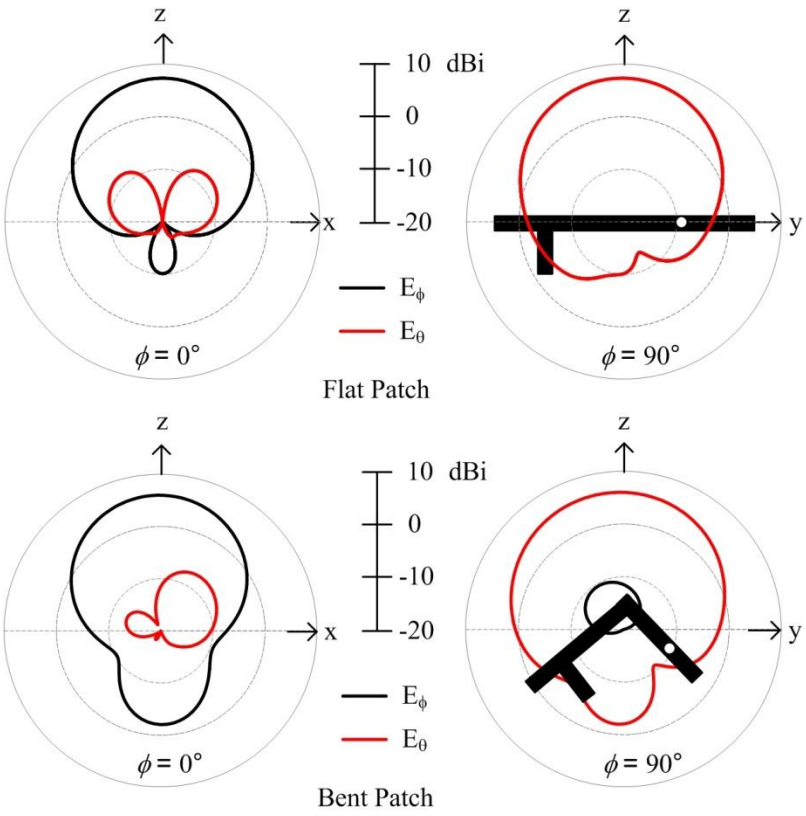

Fig. 23. Radiation patterns for EFCD-compensated patch bent 0°, W' = 0 mm (top) and bent 90º, W' = 30 mm (bottom).

In addition to compensating for the impedance effects of deformation, the EFCD mechanism also effects the beam-tilting in the y-z plane. The radiation patterns remain broad because the EFCD mechanism does not dramatically affect the relative electrical spacing between the slots. The increase of the cross-polarization in the y-z plane and its asymmetric distortion in the x-z plane are a result of one of radiating slots having two different materials along its width. Fig. 24 shows the radiation patterns if the fluid is displaced by $W' = W$. With the fluid completely displaced, the radiating slot becomes homogenous along its width and the symmetry of the radiation patterns is restored.

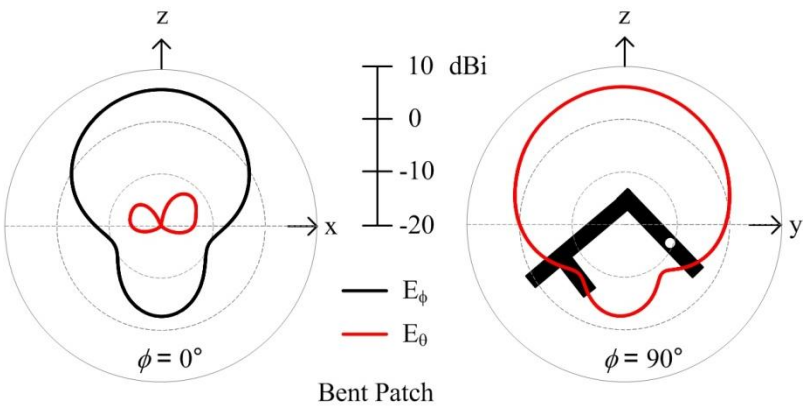

Fig. 24. Radiation patterns for EFCD-compensated patch bent 90°, W' = 37 mm.

B. Fabrication

600 nm colloidal Barium Strontium Titanate (*BSTO*) [35] ($\varepsilon_{r2} \sim 500$ and $tan\ \delta_2 \sim 0.01$) was dispersed into low-loss oil (petroleum distillate) ($\varepsilon_{r1} \sim 2.1$ and $\delta_1 \sim 0$) to make the EFCD for experiments. A volume fraction of $\vartheta = 50\%$ was chosen and this mixture was stirred vigorously 30 min. until the EFCD was a qualitatively considered a 'good' dispersion (e.g., it flowed well and did not show and aggregation). Simultaneous

experiments for related research during this stage of the design process indicated the power rule had overestimated the effective permittivity of the EFCD, but the resulting EFCD was injected into thin-walled plastic straws with an outer diameter of 3 mm. These were sealed at both ends with hot glue.

Prior to PDMS becoming available two patch antennas (flat and bent 90º) were designed, simulated, and fabricated on 4 mm thick Rochelle Foam substrate to validate the concept of an EFCD compensation mechanism. The foam has a relative permittivity near unity ($\varepsilon_r \sim 1$) and provides a rigid support for the patch antenna. Both patches were fabricated by soldering two strips of copper tape together and securing the unified piece to a milling machine board for cutting. Both patch antennas share the dimensions L = 40.5 mm, W = 50 mm, h = 4 mm; the probe is 10.5 mm from the edge opposite the capillary. The patch of the 90º antenna has an additional length dL = 5.65 mm to represent the expanded cavity (stretched conductor). Both substrates use 3 mm wide channels for the insertion of EFCD-filled straws. The edge of the channels line up with the edge of the patch. Hot glue adhered the substrate to the ground plane. Delamination of the copper tape led to the addition of foam strips along the patch edges to secure the patches' placement during measurements. Fig. 25 shows the fabricated antennas and their constitutive parameters.

Fig. 25. Flat air foam patch antenna (left) and bent air foam patch antenna (right).

C. Measurement

An Agilent 8510C Vector Network Analyzer [36] measured the input impedance of the each antenna as the EFCD straw is removed from the channel in 25% increments. As a control, the experiment was repeated using straws filled with water. Fig. 26 compares the EFCD ($\varepsilon_r \sim 9.2$) to water ($\varepsilon_r \sim 80$) by plotting the frequency shifts of the flat patch antennas. Even though the water has a much higher permittivity than the EFCD the results show little difference. This is likely due to the reconfiguration limit observed in Fig. 10 for a substrate with $\varepsilon_r = 1$. Fig. 27 shows the VSWR of the flat antenna with the EFCD, the 90º antenna with the EFCD, and the 90º antenna with the EFCD fully displaced.

As stated earlier the antenna design assumed the relative permittivity was $\varepsilon_{ro} = 25$, but the measured results indicate the actual permittivity of the material was much lower. This initial experiment highlighted the need for more precise mixing rules and

measurement systems for the currently available materials. However, despite the relatively small effects of the material perturbation in this experiment and the impedance mismatch of the flat patch, the two antennas share a small overlap in bandwidth as seen in Fig. 27.

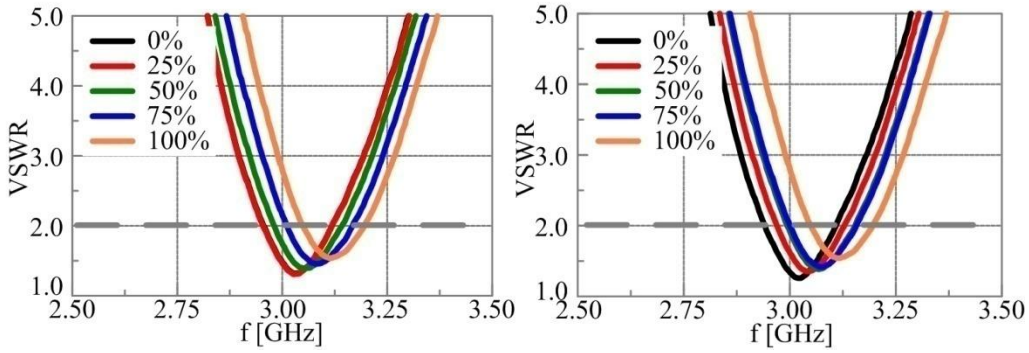

Fig. 26. VSWR of the flat antenna as EFCD is displaced (left) and as water is displaced (right).

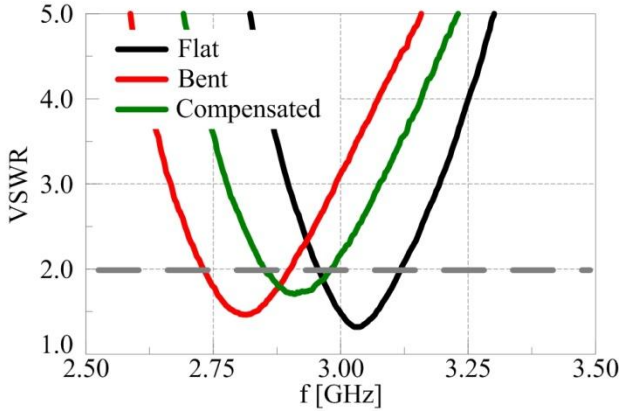

Fig. 27. VSWR of the air foam patch flat, bent, and then compensated by displacing the EFCD.

CHAPTER V

FABRICATED ANTENNA AND RESULTS II

A. Modifications

The availability of a better EFCD dispersion process (discussed later in Section 5.C), a more accurate mixing formula (6), and a material characterization system [26] led to several modifications of the design. The EFCD permittivity of ε_{ro} = 9.2 replaces the previously assumed value of ε_{ro} = 25 in the model to provide better agreement between simulated and measured results. To make the model even more accurate, a localized region of curvature has been examined in place of the sharp bend to better represent the elastic nature of PDMS. A flexible, conductive epoxy SEC 1233 [37] {$\rho \sim .0003$ Ω-cm} forms the patch metallization layers.

B. Simulation

The model dimensions are h = 4 mm, W = 37 mm, and the feed remains 6.5 mm from the edge opposite the capillary (based on the initial PDMS patch antenna design). The only dimension of the patch altered from replacing the permittivity of the EFCD is the length L. Lowering the EFCDs permittivity that initially resides in the capillary when the patch is flat decreases its contribution to the electrical length of the antenna. The physical length increases to L = 26 mm to adjust for this. The lower value of ε_{ro} in the model limits the design's capacity for compensation. Fig. 28 shows the impedance results of the EFCD-adjusted simulation. The EFCD is fully displaced (i.e. $W' = W$) but the center

frequency of the 90° case remains centered slightly to the left of 3 GHz (e.g., it is shifted down in frequency). However, this provides a compelling result that this compensation mechanism can in fact counteract the effects from bending!

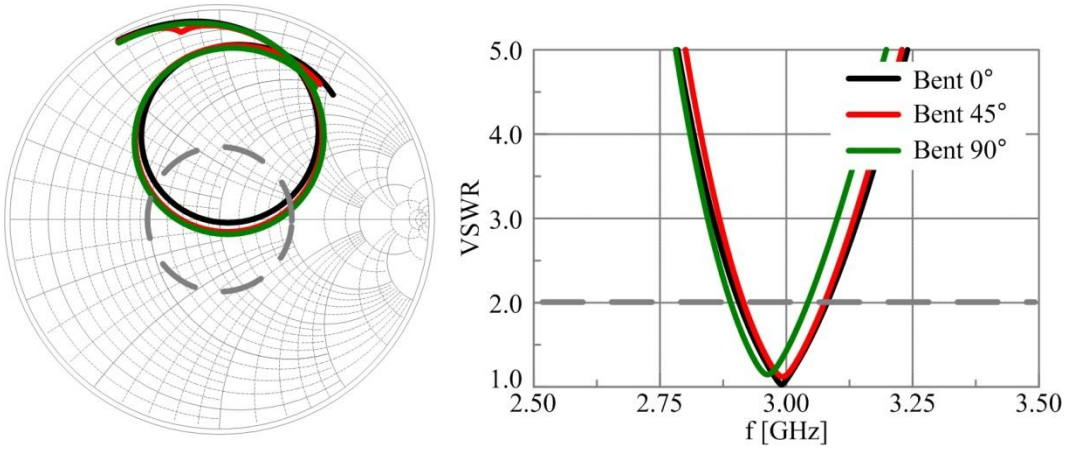

Fig. 28. Smith chart showing S_{11} for the EFCD-compensated antenna with ε_{ro} = 9.2(left) and corresponding VSWR (right).

Changing the nature of the deformation to a localized curvature (Fig. 29) creates a greater deformation effect than the sharp bend but better approximated the way a flexible material will deform. Fig. 30 shows the impedance results of the curvature-adjusted simulation. A greater deformation and a more limited compensation mechanism results in the 90° center frequency shifting even lower. As a result, the preserved bandwidth is reduced to a fraction of what it was in the initial design, but the antenna demonstrates enough bandwidth to merit fabrication.

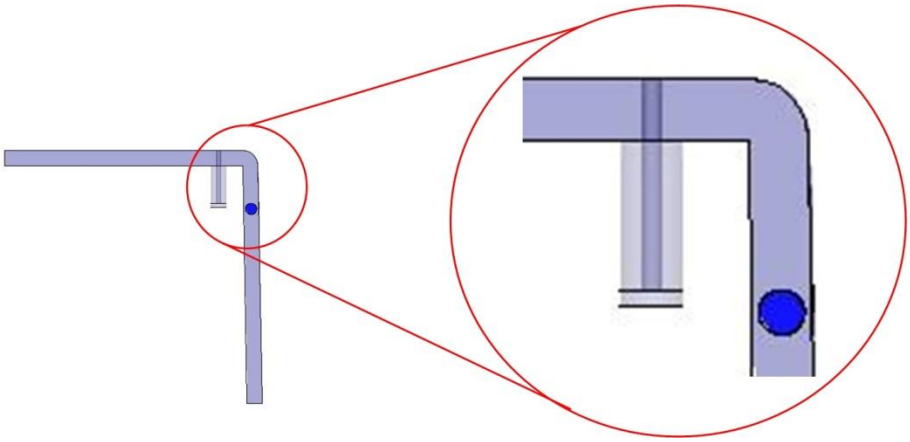

Fig. 29. Localized curvature from bending.

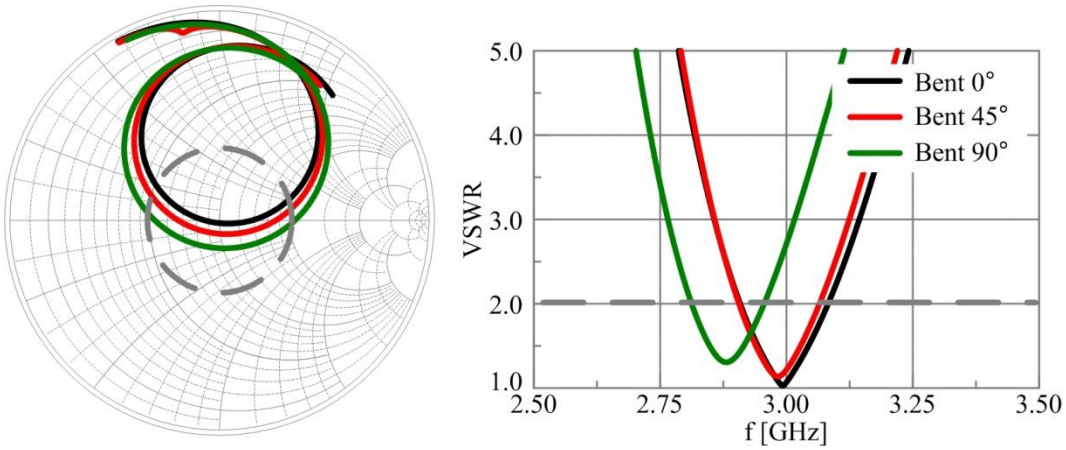

Fig. 30. Smith chart showing S_{11} for the adjusted simulation (left) and corresponding VSWR (right).

C. Fabrication

The 600 nm colloidal BSTO was treated with Nanosperse [38] surfactant ($\varepsilon_r \sim 8$ and $tan\ \delta \sim 0.11$) before being dispersed into petroleum distillate at a volume fraction of $\vartheta = 50\%$. To create a homogeneous sol, this mixture underwent a cycles of 15 min. vortexing (vigorously shaken and stirred) and 30 min. sonication (degassed and sifted) for a total

of ~ 5 hrs. A material characterization system and Maxwell-Garnett mixing rule indicated this EFCD had an ε_{reff} ~ 9.2. Since the overall volume fraction of surfactant was small (< 2.5%) this material was not included into the calculations of effective material properties. The EFCD was again injected into straws with an outer diameter of 3 mm, and the straws were sealed at both ends with hot glue.

The fabrication process in this thesis for the PDMS patch begins with a square mold for the substrate. A pair of holes drilled into opposing side-walls to suspend a thin metal rod – the negative of the capillary – above the base of the mold. The rod and the inside of the mold are coated with a thin layer of oil to prevent the PDMS from strongly adhering to the metal surfaces. Given on the dimensions of the mold, appropriate volumes of PDMS base and curing agent were measured out to provide the proper substrate thickness after curing. Once mixed the PDMS is vortexed to remove air bubbles. Prior to pouring the PDMS in the mold, hot glue provided a temporary seal between the metal rod and the holes to prevent the PDMS from seeping through. Once the PDMS is poured mold it is cured at 100° C for one hour. Once cooled, the hot glue was removed and then the metal rod pulled out to provide the circular capillary.

A printed layout of the antenna mapped the location of the probe; the probe was inserted into the PDMS substrate and superglued to ensure adhesion prior to applying the SEC 1233 conductive epoxy. The SEC 1233 was mixed in a ventilation hood and brushed across a mask laid on top of the PDMS to create the patch. The entire ground plane is

coated to ensure contact with the probe. The PDMS and the SEC 1233 are cured at 60° C for one hour. Fig. 31 shows the fabricated antenna.

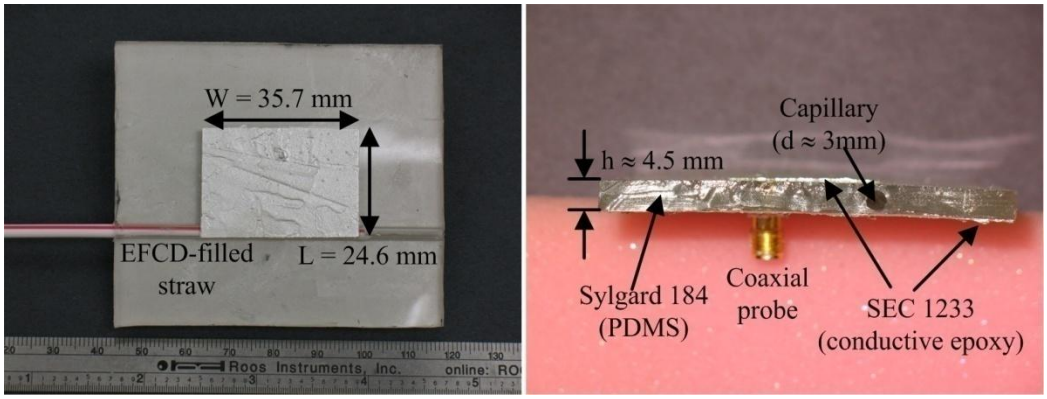

Fig. 31. Top view of PDMS antenna (left) and cross-sectional view of PDMS antenna (right).

D. *Measurement*

The flexible patch antenna was measured using the same equipment as the air foam patch antennas. Measurements were obtained for 0% ($W' = 0$) and 100% ($W' = W$) displacement of the EFCD in the flat state. Delamination of the patch due to deformation and tears in the capillary walls due to friction with the EFCD-filled straw prevented further experimentation. Fig. 32 shows the effect of displacing the EFCD on the impedance match. As can be seen from the shift in center frequency and the contraction of the impedance locus, the patch antenna experiences a length reduction on one side of the probe, corroborating the measured results from the previous experiment.

The antenna detuned from the design frequency as a result of differences between the fabricated and design dimensions. A small excess in the volume of PDMS poured

resulted in a slightly thicker substrate; however, the variation in substrate thickness only slightly detunes the antenna. The majority of the error resulted from inaccurate patch dimensions. The patch width W and length L were both ~1.5 mm shorter than the dimensions specified in the design. The size reduction of the patch resulted from the curing process for the SEC 1233 [39]. Fig. 33 compares the VSWR of the design, the measured data, and a model with dimensions equal to those of the fabricated patch. The agreement between the measured results and the adjusted model suggests the errors result from the fabrication.

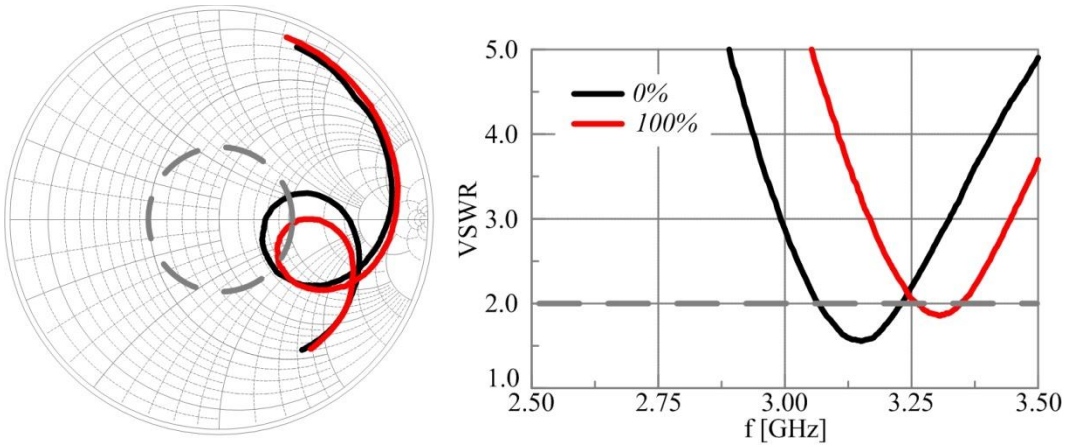

Fig. 32. Smith chart showing S_{11} for the measured flat PDMS antenna (left) and corresponding VSWR (right).

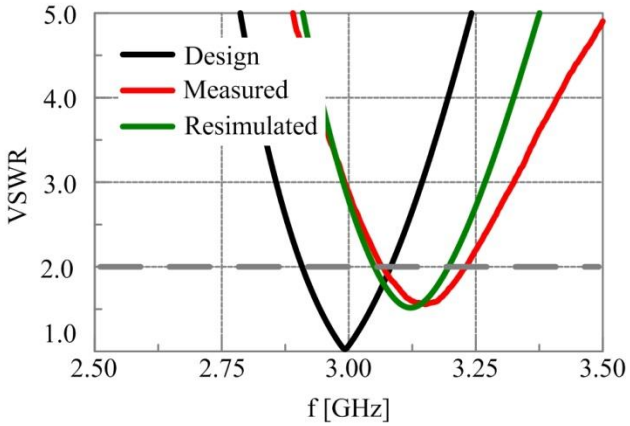

Fig. 33. *VSWR* comparison of the design, the measured results, and a resimulated model.

CHAPTER VI

CONCLUSION

A. *Summary*

Beginning with a fundamental background behind the antennas and material perturbation technique used in this work, this thesis has examined a sharp bend in the middle of a microstrip patch antenna. The effects of this deformation on the impedance and radiation behavior of the antenna were also addressed. Both theoretical considerations and simulated results indicate that the deformation acts as a length extension in the resonant direction. The simulated model first examined a probe-fed patch antenna on 4 mm thick Sylgard 184. In the initial (flat) state, the patch operates at f_o = 3 GHz. As the bend angle increases up to 90º, the resonant frequency decreases and the Smith chart locus broadens, completely detuning the antenna at a bend angle of 45º.

This work then examined a material perturbation to compensate the effect of deformation. Specifically, the mechanism provided a length reduction effect by displacing a high permittivity EFCD with a low permittivity EFCD via a capillary embedded in the substrate of the antenna. Modeling the EFCD capillary in a microstrip patch cavity and applying approximations based on the capillary size, this thesis presents an expression for the shift in resonant frequency as a result of material displacement in the capillary. Simulation of a flat patch antenna with the EFCD capillary validates the

assumption that this perturbation acts as a length reduction: the center frequency increases and the Smith chart locus contracts.

Since the impedance effects of material perturbation oppose the effects of deformation, the EFCD capillary may be used as a compensation mechanism. In the design presented, antenna deformation actuates an EFCD compensation mechanism. A simulated model featuring both the deformation and the EFCD capillary displacement evaluates this compensation mechanism. The high permittivity EFCD in the model, which is displaced by air ($\varepsilon_r \sim 1$), has permittivity $\varepsilon_r = 25$. Tuning the fluid displacement to the bend angle preserves 141 MHz of bandwidth even as the antenna bends up to 90º.

Based on available materials and fabrication methods, two microstrip patch antennas were fabricated on Rochelle Foam ($\varepsilon_r \sim 1$); one antenna representing the flat state and the other representing the expanded bent state. Both antennas feature a channel through which an EFCD-filled straw can slide in and out representing EFCD displacement. The measured results follow the same trends as the simulated results, but the fabricated antennas do not have the same input impedance as the simulated model. The differences between simulation and fabrication highlighted the need for an alternate fabrication process, a more accurate mixing rule for EFCD preparation, and a material characterization system [26].

As more materials became available, the simulated model adjusted to better represent the physical antenna and a second design was fabricated using Sylgard 184 as a substrate and conductive epoxy for the metallization layers. The EFCD displaced in the new design used a volume fraction of 50% BSTO ($\varepsilon_{r2} \sim 500$ and $tan\ \delta_2 \sim 0.01$) that was treated with Nanosperse surfactant ($\varepsilon_r \sim 8$ and $tan\ \delta \sim 0.11$) and dispersed in petroleum distillate ($\varepsilon_{r1} \sim 2.1$ and $\delta_1 \sim 0$). Antenna measurements in the flat state followed the same trend as the simulated results, but the impedance match was degraded as a result of epoxy shrinking during the curing process. The epoxy also delaminated with deformation and the insertion of an EFCD-filled straw tore the capillary walls. These defects prevented antenna measurements of the bent state and highlight the need for alternate materials and delivery systems.

B. *Future Work*

The compensation mechanism in this thesis employs a cylindrical capillary filled with dielectric fluid, but the design space for compensation mechanisms is only limited by the diversity of material properties and perturbation methods. As new materials and enabling technologies become available this work will develop new topologies.

The EFCD used in this work is a 50% volume fraction of BSTO, a spherical colloid. The Maxwell Garnett rule for spherical colloids (6) and Fig. 12 indicate the initial design in this work ($\varepsilon_{ro} = 25$) requires a higher volume fraction of BSTO than our currently available mixing methods can produce. Realizing this design requires improved mixing

methods (poly-dispersed systems), new materials (higher ε_r), or alternate colloidal geometries (e.g. discs, whiskers).

In addition, the topology in this thesis is limited by a decrease in field strength as a result of the electric field being perpendicular to the capillary axis [32]. However, the magnetic field in the fundamental TM_{10} mode is parallel to this axis and not limited by the same field effects. The availability of low-loss magnetic ($\Delta\mu$) EFCDs coupled with displacement through a capillary in the middle of the patch (where the visibility of magnetic particles is the greatest) may provide a stronger compensation mechanism.

REFERENCES

[1] Drake, F. H., "An aircraft radio receiver for use with rigid antenna," in *Proc. of the IRE*, vol. 17, pp. 306-319, 1929.

[2] Friedberg, M. R., "Mobile antennas for vehicular communications," *Transactions of the IRE Professional Group on Vehicular Communications*, vol. 1, pp. 100-104, 1952.

[3] Webster, R., "20-70 MC monopole antennas on ground-based vehicles," *Antennas and Propagation, IRE Transactions on*, vol. 5, pp. 363-368, 1957.

[4] Munson, R. E., "Conformal antennas for smart cars," in *Aerospace Applications Conference, 1994. Proc., 1994 IEEE*, 1994, pp. 325-332.

[5] Knott, P., "Antenna design and beamforming for a conformal antenna array demonstrator," in *Aerospace Conference, 2006 IEEE*, 2006, p. 7 pp.

[6] Granger, J. V. N., "Shunt-excited flat-plate antennas with applications to aircraft structures," in *Proc. of the IRE*, vol. 38, pp. 280-287, 1950.

[7] Goetz, A. C. and Chea, H. K., "Conformal Load-bearing Antenna System that Excites Aircraft Structure," U.S. Patent no. 6097343, Oct. 23, 1998.

[8] Tuss, J., Lockyer, A., Alt, K., Uldrich, F., Kinslow, R., et al., "Conformal loadbearing antenna structure," in AIAA/ASME/ASCE/AHS/ASC Structures, Structural Dynamics and Materials Conference and Exhibit Salt Lake City, UT: American Institute of Aeronautics, Inc., 1996, pp. 836-843.

[9] Camacho, G. I. and Campbell, D. V., "Multifunction Structurally Integrated VHF-UHF Aircraft Antenna System " U.S. Patent no. 5825332, Sept. 12, 1996.

[10] Huff, G. H. “A structurally functionalizable spiral aperchassis,” in Proc. 2008 Antenna Applications Symposium, Allerton Park, Monticello, IL, Sept., 2008, pp. 426-435.

[11] VanBlaricum, M. L., Larry, T. L., Huff, G. H., “A design approach for reconfigurable RF surfaces and apertures,” in Society of Engineering Science: 45th Annual Technical Meeting, Champaign, IL, Oct. 13-15, 2008.

[12] Nechayev, Y. I., Hall, P. S., Constantinou, C. C., Yang, H., Alomainy, A., et al., "On-body path gain variations with changing body posture and antenna position," in *Antennas and Propagation Society International Symposium*, 2005 IEEE, 2005, pp. 731-734 vol. 1B.

[13] DeVaul, R., Gips, J., and Sung, M., "The MIThril Project." MIT Media Lab. http://www.media.mit.edu/wearables/mithril (accessed April 19, 2009).

[14] Steyskal, H. "Pattern synthesis for a conformal wing array," in *Aerospace Conference Proc., 2002. IEEE*, 2002, pp. 2-819-2-824 vol.2.

[15] Callus, P. J., "Conformal load-bearing antenna structure for Australian Defence Force aircraft," in Air Veh. Div., Def. Sci. and Tech. Org., Fishermans Bend, Victoria, Australia. Rep. DSTO-TR-1963, March 2007.

[16] Hemming, L., Kovalchik, M., and Johnson, D. "Conformable, integrated antenna structure providing multiple radiating apertures," U.S. Patent no. 6121936, Sept. 19, 2000.

[17] Smallwood, B. P., "Structurally Integrated Antennas on a Joined-Wing Aircraft," M.S. thesis, Dept. of Aeronautics and Astronautics, Air Force Institute of Technology, Wright-Patterson Air Force Base, OH, 2003

[18] Raburn, L. E., "A very-high-frequency ultra-high-frequency tail-cap Antenna," in *Proceedings of the IRE*, vol. 39, pp. 656-659, 1951.

[19] Anstey, M. and Saoudy, S. A., "Radiation characteristics of a ship-mounted high frequency ground wave radar antenna," in *Antennas and Propagation Society International Symposium, 1996. AP-S. Digest*, 1996, pp. 1852-1855 vol.3.

[20] Cravey, R. L., Vedeler, E., Goins, L., Young, W. R. and Lawrence, R.W., "Structurally Integrated Antenna Concepts for HALE UAVs," Langley Research Center, Hampton, VA, Tech. Memo. NASA/TM-2006-214513, Oct. 2006.

[21] Kabacik, P. and Kucharski, A., "The effect of conformality on the electrical properties of small antennas," in *Antennas and Propagation Society International Symposium, 2001. IEEE, 2001,* pp. 50-53 vol.3.

[22] Haugse, E. D., Ridgway, R.I., Hightower, C.H, and Warren, R. C., "Structural Deformation Compensation System for Large Phased-array Antennas," U.S. Patent no. 6333712, Dec. 25, 2001.

[23] Dahele, J. S., Mitchell, R. J., Luk, K. M. and Lee, K. F., "Effect of curvature on characteristics of rectangular patch antenna," *Electronics Letters,* vol. 23, pp. 748-749, 1987.

[24] Koulouridis, S., Kiziltas, G., Zhou, Y., Hansford, D. J. and Volakis, J. L. "Polymer–ceramic composites for microwave applications: fabrication and performance assessment," *Microwave Theory and Techniques, IEEE Transactions on*, vol. 54, pp. 4202-4208, 2006.

[25] Huff, G. H., Bahukudumbi, P., Everett, W. N., Beskok, A., Bevan, M. A., et al., "Electromagnetically tunable fluids for microfluidic reconfiguration of antennas," in Proc. 2007 URSI North American Radio Science Meeting, Ottawa, ON, Canada, July 2007.

[26] Huff, G. H. and Goldberger, S., "A coaxial stub microfluidic impedance transformer (COSMIX)," in review *IEEE Microw. Wireless Compon. Lett*., submitted March, 2008.

[27] Huff, G. H. and Goldberger, S., "Integration of vascular reconfiguration mechanisms in a microstrip patch antenna," in review *IEEE Antennas Wireless Propag. Lett.*, submitted March, 2008.

[28] Lichtenecker, K., *Physikalische Zeitschrift*. 1926. p. 117

[29] Sihvola, A. H. *Electromagnetic Mixing Formulas and Applications*. UK: Institution of Electrical Engineers, 1999, p.164

[30] Balanis, C. A. *Antenna Theory: Analysis and Design*. 3rd ed. Hoboken, NJ: John Wiley & Sons, Inc., 2005.

[31] Harrington, R. F. *Time-Harmonic Electromagnetic Fields*. New York: John Wiley & Sons, Inc., 2001. pp. 321-324

[32] Smythe, W. R. *Static and Dynamic Electricity*, 2nd ed. New York: McGraw-Hill Book Company, Inc., 1950. pp. 67-68.

[33] Ansoft, HFSS© v11.1, Pittsburgh, PA.

[34] Dow Corning Corp., Sylgard© 184 Silicone Elastomer Kit, Midland, MI.

[35] TPL, Inc., NanOxide™ HBS 1000 Barium Strontium Titanate Powder, Albuquerque, NM.

[36] Agilent Technologies, 8510C Vector Network Analyzer, Santa Clara, CA.

[37] ResinLab L.L.C., SEC 1233, Germantown, WI.

[38] TPL, Inc., Nanosperse© 484 Wetting & Dispersion, Albuquerque, NM.

[39] Wentworth, S. M., Dillaman, B. L., Chadwick, J. R., Ellis, C. D. and Johnson, R. W., "Attenuation in silver-filled conductive epoxy interconnects," *Components, Packaging, and Manufacturing Technology, Part A, IEEE Transactions on,* vol. 20, pp. 52-59, 1997.

VITA

Stephen Andrew Long
friendlyaggie@neo.tamu.edu
323 Zachry Engineering Center
College Station, TX 77843-3128

Professional Preparation

B.S., Electrical Engineering, Texas A&M University, Dec. 2006

M.S., Electrical Engineering, Texas A&M University, May 2009

Appointments and Research Experience

Teaching assistant, ECE Department, Texas A&M Univ., Spring 2009

Student engineer, Naval Research Lab, Radar Division, June 2008 to date

Research assistant, EM Lab, ECE Department, Texas A&M Univ., 2007 to date

Undergraduate researcher, EM Lab, ECE Department, Texas A&M Univ., Fall 2006

Senior Design Project: Force-sensitive controller for adjusting elevation angle for hospital beds (PCB design, bed construction, motor and AC drive installation), Fall 2006

Conference Papers and Other Public Speaking

[1] Long, S. A. and Huff, G. H., "Dynamic compensation mechanisms for deformable radiating structures based on colloidal dielectrics and fluidics," in *Proc. of 2009 SPIE Smart Structures and Materials & Nondestructive Evaluation and Health Monitoring*, San Diego, CA, March 2009

[2] Huff, G. H., Goldberger, S., and Long, S. A.,"The RF cuttlefish: overview of biologically inspired concepts for reconfigurable antennas and smart skins," in *Proc. 2008 Antenna Applications Symposium*, Allerton Park, Monticello, IL, Sept. 2008, pp. 395 – 415.

[3] Long, S. A. and Huff, G. H., "A study of microfluidic compensation mechanisms for deformable antennas," in *Proc. 2008 URSI General Assembly*, Chicago, IL, Aug. 2008.

[4] Long, S. A. and Huff, G. H., "Microfluidic compensation mechanisms for polymorphic structures," (invited talk) Naval Research Lab, Radar Division, Washington, DC, March 5, 2008.